Numerical Simulation of the Time-Fractional Fokker–Planck Equation and Applications to Polymeric Fluids

Jonas Beddrich[a,*], Endre Süli[b], Barbara Wohlmuth[a]

[a] *Department of Mathematics, Technical University of Munich, 85748 Garching, Germany*
[b] *Mathematical Institute, University of Oxford, Woodstock Road, Oxford OX2 6GG, UK*

Abstract

We introduce a new approach to the numerical approximation of the time-fractional Navier–Stokes–Fokker–Planck (TFNSFP) system, which involves the coupling of the incompressible Navier–Stokes equations to a time-fractional Fokker–Planck equation. The model arises in the context of dilute polymeric fluids, and it enhances the standard integer-derivative version of the model by including memory effects. The key challenge associated with the numerical solution of the TFNSFP system is that, in addition to it being nonlocal in time, it is, even in its simplest form, posed on a spatial domain that is the Cartesian product of two d-dimensional domains, for $d \in \{2, 3\}$, the d-dimensional flow domain and the d-dimensional configuration space domain. We combine a kernel compression technique based on rational approximation of the integral kernel of the time-fractional derivative with a space-splitting method. By doing so, we transform the time-fractional partial differential equation into a fixed number of integer-order in time partial differential equations. The Fokker–Planck equation posed on the $2d$-dimensional domain is decoupled into two d-dimensional problems, and a standard combination of the Hermite spectral method on the configuration space domain and a finite element method on the flow domain is then applied. Finally, we combine our numerical scheme for the time-fractional Fokker–Planck equation (TFFPE) with a standard Navier–Stokes solver. We propose an efficient implementation strategy based on the algebraic structure of the discretized time-fractional Fokker–Planck equation, which significantly reduces the computational cost.

Keywords: Navier–Stokes–Fokker–Planck system, numerical simulation, time-fractional PDE, Hermite spectral method, dilute polymeric fluids, Hookean bead-spring-model

1. Introduction

The flow of a polymeric fluid inherently differs from that of a Newtonian fluid, e.g., turbulent flow can occur even at low Reynolds numbers [1]. Adding polymer molecules to an otherwise Newtonian fluid results in a viscoelastic fluid, which exhibits both viscous and elastic behavior [2]. Here, we shall be concerned with a

*Corresponding author
Email address: beddrich@ma.tum.de (Jonas Beddrich)

particular class of models of dilute polymeric fluids, which involves the coupling of the incompressible Navier–Stokes equations to a time-fractional Fokker–Planck equation (FPE), and we shall introduce a numerical scheme for its approximate solution.

Originally, Fokker and Planck derived the FPE to model the Brownian motion of particles [3, 4]. In general, the FPE describes the evolution of a probability density function ψ under the influence of drift and diffusion, and thus, finds applications in numerous fields such as solid-state physics [5], quantum optics [6], molecular biology [7], and it is also used to model the viscoelastic properties of polymeric fluids.

In the context of polymeric fluids the FPE has been widely studied analytically and from the computational point of view. For a recent overview, we refer to [8], and to [9] for a review of the related Oldroyd-B model. Commonly, one considers long polymer molecules within a viscous incompressible Newtonian solvent, neglecting self-interaction of the polymer molecules as well as interactions between different polymer molecules, such as entanglement. In the simplest case, a single polymer molecule is modeled as a pair of massless beads that are connected with an elastic spring. In this, so-called, *dumbbell model* each polymer molecule is represented by its end-to-end vector, the so-called configuration vector, which corresponds to the orientation vector of the elastic spring connecting the pair of massless beads. Different models arise depending on the degree to which the polymer molecules can be extended. Finitely extensible nonlinear elastic (FENE) models involve a spring-force defined on a bounded open ball in $\mathbb{R}^d$, $d \in \{2, 3\}$, as configuration space, see, e.g., [10, 11], while the Hookean model allows for polymer molecules of arbitrary length, as discussed in [12, 13] and involves a linear spring force defined on the whole of $\mathbb{R}^d$. In the latter case, suitable decay conditions need to be imposed to avoid the nonphysical scenario of infinitely long polymer molecules. This modeling assumption is widely used in practice because of its simplicity [13]. We shall confine ourselves here to such a Hookean model.

We consider the following formulation of the FPE. Let $\Omega \subset \mathbb{R}^d$ be a bounded and open domain, $\mathcal{D} = \mathbb{R}^d$, and $T \in \mathbb{R}_+$. We denote the configuration vector of the polymer molecule with $\mathbf{R} \in \mathcal{D}$, and $\mathbf{x} \in \Omega$ is the spatial variable. The probability density function $\psi(t, \mathbf{x}, \mathbf{R})$ satisfies the following FPE in $(0, T] \times \Omega \times \mathcal{D}$:

$$\partial_t \psi = F(\psi) := - \mathbf{u} \cdot \nabla_x \psi + \epsilon \Delta_x \psi - \nabla_R \cdot (\tau(\mathbf{u}) \cdot \mathbf{R}\psi) + \nabla_R \cdot (\xi \mathbf{R}\psi) + \chi \Delta_R \psi, \tag{1}$$

where $\mathbf{u} : [0, T] \times \overline{\Omega} \to \mathbb{R}^d$ denotes the velocity field of the fluid, $\epsilon > 0$ the center-of-mass diffusion coefficient, $\xi > 0$ is the spring constant, $\xi \mathbf{R}$ represents the Hookean spring force, see, e.g., [14], and $\chi > 0$ is the diffusion coefficient for the configuration space. The drag term $\tau(\mathbf{u})$ is commonly either the spatial gradient of the velocity $\tau(\mathbf{u}) \coloneqq \nabla_{\mathbf{x}} \mathbf{u}$ (resulting in the so-called *general noncorotational model*) or its corotational part $\tau(\mathbf{u}) \coloneqq \frac{1}{2}(\nabla_{\mathbf{x}} \mathbf{u} - (\nabla_{\mathbf{x}} \mathbf{u})^{\mathrm{T}})$ (resulting in the so-called *corotational model*).

Both choices for $\tau(\mathbf{u})$ have been widely studied in the literature. Concerning the general noncorotational model, we refer to [15] for an introductory review, to [16] for the compressible isentropic case, to [13] for the incompressible case, and to [17] for the global existence of weak solutions. For studies of the corotational model, we refer to [18] for the existence of weak solutions of the FENE-dumbbell model, to [19, 20] for the

well-posedness of the model in 2D, to [21] for the analysis of the time-decay of solutions, to [22] for the numerical approximation, and to [23] for a recent analysis of the existence of solutions.

For the FPE, defined on the Cartesian product of the spatial domain Ω and the configuration space domain $\mathcal{D}$, the underlying idea of most numerical schemes is to treat the problem on each domain separately. This so-called space-splitting approach (also known as the alternating-direction method) was introduced in [24] and the first rigorous numerical analysis was performed in [25]. Commonly, one uses a combination of a spectral method over the configuration space and a finite element method over the physical space. For FENE-type models, a Galerkin spectral method based on spherical harmonics can be used (see, e.g., [25, 26]), while a Hermite spectral method can be used for Hookean models, see [27, 12]). Since ψ is, by definition, a probability density function and is therefore nonnegative, specialized structure-preserving numerical methods have also been used, see, e.g., [28, 29].

Time-fractional differential equations have grown in popularity because they can accurately describe various physical phenomena. Their advantage lies in their nonlocality in time since they consider all previous states of the solution as so-called memory effects. From a purely mathematical point of view, the FPE could be generalized by replacing the time derivative on the left-hand side with a time-fractional derivative of Caputo-type. It was shown in [30] however that the derivation of the time-fractional Fokker–Planck equation (TFFPE) from the Langevin equation places the time-fractional derivative of Riemann–Liouville-type inside the spatial differential operator appearing, instead, on the right-hand side of the FPE, leaving the integer-order time-derivative on the left-hand side of the FPE unchanged. These differing formulations of the FPE are only equivalent in the special case of a time-independent operator F, i.e., when the velocity field $\mathbf{u}$ involved in F is time-independent, see [31].

The time-fractional Fokker-Planck equation under consideration here therefore reads as follows:

$$\partial_t \psi = F(\partial_t^{1-\alpha} \psi), \tag{2}$$

where $\alpha \in (0, 1]$, and the time-fractional derivative $\partial_t^{1-\alpha}\psi$ is of Riemann–Liouville type. It is defined as $\partial_t^{\alpha} f(t) := \partial_t \mathcal{I}^{1-\alpha} f(t)$, where $\mathcal{I}^{\alpha}$ is the Riemann–Liouville fractional integral operator of order $\alpha \in (0, 1]$ on $L_1(0, T)$, see, e.g., [32]. It is given by

$$\mathcal{I}^{\alpha} f(t) := \int_0^t K_{\alpha}(t - s) f(s) ds, \quad 0 \le t \le T, \tag{3}$$

where the integral kernel reads as $K_{\alpha}(t) := t^{\alpha-1}/\Gamma(\alpha)$ and $\Gamma(\cdot)$ is the gamma function. For an introduction to the theory of time-fractional derivatives, we refer to [32]. We postpone the discussion of the choice of the initial condition and of the boundary conditions to Section 2.1.

The majority of numerical methods for time-fractional derivatives are either quadrature schemes for the convolutional integral or approximation schemes for the integral kernel. The former include the L1 scheme (see, e.g. [33, 34]) and fractional linear multi-step methods [35], most-notably Adams–Moulton/Bashforth type schemes (see, e.g. [36]). Standard quadrature schemes suffer from nonlocality, i.e., the required storage

grows linearly and the computational complexity quadratically with the number of time steps. Approximation schemes for the integral kernel include kernel compression techniques that approximate the integral kernel with a sum of exponentials (see, e.g., [37], and more specifically for $t^{-\alpha}$ [38]), as well as techniques that use multipole polynomial interpolations of the kernel spectrum [39]. A detailed overview of numerical methods for time-fractional differential equations can be found in [40].

Various numerical methods have been successfully applied to different versions of the TFFPE, including ones based on the Laplace transform [41], the predictor-corrector approach from [36] in [42], the variational iteration method [43], the Adomian decomposition method [43], finite differences [44, 45], the L1-method [46], the multistep reduced differential transformation method [47], as well as the fractional power series method [48]. All of the publications mentioned above consider the TFFPE confined to the configuration space. Because of the associated computational cost, see, e.g., [44], it is unclear how any of these techniques can be applied to a TFFPE defined over the Cartesian product of two d-dimensional domains, $d \geq 2$, as is the case in the model under consideration here.

While the TFFPE describes the behavior of the polymer molecules, the movement of the fluid into which the polymer molecules are immersed is modeled by the incompressible Navier–Stokes equations (NSE). The Navier–Stokes system is coupled to the Fokker–Planck equation through the presence of the velocity field, $\mathbf{u}$, in the TFFPE, while the probability density function, ψ, enters into the NSE through an additional polymeric/elastic stress tensor $\mathbf{T}$, which is given by the so-called Kramers expression $\mathbf{T} \coloneqq \mathbf{C} - \gamma \mathbf{Id}$, see, e.g., [17], where γ is in general a function defined on $[0,T] \times \overline{\Omega}$ that can depend on the polymer number density, $\int_{\mathcal{D}} \psi(t, \mathbf{x}, \mathbf{R})\, d\mathbf{R}$, but is, for the sake of simplicity, considered to be constant in this work, and

$$\mathbf{C} \coloneqq \int_{\mathcal{D}} \partial_t^{1-\alpha} \psi(t, \mathbf{x}, \mathbf{R}) \mathbf{R}\mathbf{R}^{\mathrm{T}} d\mathbf{R}. \tag{4}$$

Thus, we seek a velocity field $\mathbf{u} : \overline{\Omega} \times [0,T] \to \mathbb{R}^d$ and a pressure $p : \Omega \times (0,T] \to \mathbb{R}$ that satisfy

$$\partial_t \mathbf{u} + \mathbf{u} \cdot \nabla \mathbf{u} = -\nabla p + 2\nu \nabla \cdot \mathbf{D}(\mathbf{u}) + \nabla \cdot \mathbf{T}, \tag{5}$$

$$\nabla \cdot \mathbf{u} = 0, \tag{6}$$

where $\nu > 0$ is the viscosity coefficient and $\mathbf{D}(\mathbf{u}) \coloneqq \frac{1}{2}(\nabla_{\mathbf{x}} \mathbf{u} + (\nabla_{\mathbf{x}} \mathbf{u})^{\mathrm{T}})$ is the symmetric velocity gradient. In [30], the global-in-time existence of large-data weak solutions to a corotational, FENE-type TFNSFP system is shown for $\alpha \in \left(\frac{1}{2}, 1\right)$. For the general noncorotational model, the proof of the existence of weak solutions remains an open problem in the time-fractional case.

The paper is structured as follows. In Section 2, we discuss the mathematical model under consideration in more detail, elaborate on the choice of initial and boundary conditions, and on the difference between the corotational and noncorotational models. In Section 3, we introduce the essential algorithmic components, namely, the Hermite spectral method and the kernel compression based on rational approximation. In Section 4, we present the numerical method used to discretize the TFFPE. A kernel compression technique based on rational approximation transforms the time-fractional differential equation into m integer-order differential

equations. The space-splitting approach decomposes the system into its physical and configuration space parts. The Hermite spectral method and the finite element method are used to discretize the unbounded configuration space $\mathcal{D} = \mathbb{R}^d$ and the physical domain Ω, respectively. We then present the complete numerical method as the key contribution of this work. Section 5 is concerned with the numerical computation of the Kramers tensor. We show that for $d = 2$ (resp. $d = 3$), four (resp. seven) Hermite spectral modes suffice to calculate the velocity field and the pressure. In Section 6, we verify our numerical scheme by comparing our results for the TFFPE against an analytical solution. Further, we show the difference between the corotational and the noncorotational formulations and we investigate the influence of the order α of the time-fractional derivative on the evolution of the solution. For the TFNSFP system, we validate our theoretical findings with numerical results and show the impact of memory effects on the flow of dilute polymeric fluids. We close by providing a conclusion in Section 7.

2. Discussion of the Mathematical Model

In this section, we discuss the mathematical model considered in this work. First, we examine the TFFPE for a given velocity field $\mathbf{u}$, before elaborating on the full TFNSFP system. We also examine the influence of $\tau(\mathbf{u})$ and compare the corotational case to the general noncorotational case where the full gradient of the velocity field instead of just its skew-symmetric part, is used in the TFFPE.

2.1. Time-fractional Fokker–Planck equation

Let the velocity field $\mathbf{u}$ be given. The TFFPE is closed by a natural boundary condition on the boundary $\partial\Omega$ of the spatial domain Ω:

$$\left(\epsilon\nabla_{\mathbf{x}}\partial_t^{1-\alpha}\psi + \partial_t^{1-\alpha}\psi\mathbf{u}\right)\cdot\mathbf{n}_{\partial\Omega} = 0, \quad \text{on } (0,T)\times\partial\Omega\times\mathcal{D}, \tag{7}$$

and a sufficiently strong decay condition as $|\mathbf{R}| \to \infty$. Recall that in the Hookean model under consideration the configuration domain $\mathcal{D} = \mathbb{R}^d$, $d \in \{2, 3\}$, and $\mathbf{R}$ is the distance between the two endpoints of a polymer molecule. Thus, the decay condition can be interpreted as the probability of the presence of infinitely long polymer molecules being zero. While we do not specify the decay conditions here, later, through the choice of basis functions, our numerical approximation of the solution will be forced to decay exponentially fast as $|\mathbf{R}| \to \infty$.

The initial condition $\psi(0, \mathbf{x}, \mathbf{R}) = \psi^0(\mathbf{x}, \mathbf{R})$ specifies the initial distribution of polymer molecules within $\Omega \times \mathcal{D}$. Accordingly, we consider $\psi^0 \geq 0$ and assume that $\int_{\mathcal{D}} \psi^0(\mathbf{x}, \mathbf{R})d\mathbf{R} = 1$ for all $\mathbf{x} \in \Omega$, i.e., our initial condition results in a constant polymer number density in Ω. Assuming no inflow or outflow of polymer molecules, the amount of polymer molecules should remain constant in Ω. This is, in fact the case if $\mathbf{u} \cdot \mathbf{n}_{\partial\Omega} = 0$ at the boundary of Ω. The initial, boundary, and decay conditions of ψ ensure that $1 = \int_{\mathcal{D}} \psi(t, \mathbf{x}, \mathbf{R})d\mathbf{R}$, for all $t \in [0, T]$, see e.g. Lemma 3.2. in [15]. For the convenience of the reader, we outline the argument here. We integrate equation (2) and the boundary condition (7) over the configuration

space $\mathcal{D}$ and obtain a parabolic equation in $\zeta(t,\mathbf{x}) \coloneqq \int_{\mathcal{D}} \psi(t,\mathbf{x},\mathbf{R})d\mathbf{R}$ subject to a homogeneous Neumann boundary condition on $\partial\Omega$ and initial condition $\zeta(0,\mathbf{x}) = 1$. Provided that $\mathbf{u}$ is sufficiently smooth, this problem has a unique solution: the constant function $\zeta(t,\mathbf{x}) \equiv 1$, and the result follows.

Furthermore, we assume that the initial datum satisfies $\psi^0(\mathbf{x},\mathbf{R}) = \psi^0(\mathbf{x},-\mathbf{R})$ which then in turn yields $\psi(t,\mathbf{x},\mathbf{R}) = \psi(t,\mathbf{x},-\mathbf{R})$. This symmetry property of the solution results directly from the model assumptions and can be exploited in our numerical algorithm.

In the literature, there are two prevalent versions of the Fokker–Planck equation: the general noncorotational model, where $\tau(\mathbf{u}) = \nabla_{\mathbf{x}}\mathbf{u}$, and the corotational model, where $\tau(\mathbf{u}) = \frac{1}{2}(\nabla_{\mathbf{x}}\mathbf{u} - (\nabla_{\mathbf{x}}\mathbf{u})^{\mathrm{T}})$, see the references provided in the introduction. The corotational model restricts the influence of the solvent fluid on the polymer molecules to rotations and neglects any lengthening or shortening. We state this more rigorously in the form of the following lemma.

Lemma 1. *Let $\tau(\mathbf{u}) = \frac{1}{2}(\nabla_{\mathbf{x}}\mathbf{u} - (\nabla_{\mathbf{x}}\mathbf{u})^{\mathrm{T}})$, and suppose that the initial datum $\psi^0(\mathbf{x},\mathbf{R})$ is rotationally symmetric with respect to the conformation vector $\mathbf{R}$. Then, the TFFPE has a solution that is rotationally symmetric with respect to $\mathbf{R}$.*

Proof. We restrict ourselves to the case of $d = 2$; the proof for $d = 3$ follows along the same lines. It is sufficient to show that for a sufficiently smooth $\phi(t,\mathbf{x},\mathbf{R})$ which is rotationally symmetric in $\mathbf{R}$ also $F(\phi)$ with $F(\cdot)$ defined by (1) is rotationally symmetric.

Let $\phi(t,\mathbf{x},\mathbf{R}) = \hat{\phi}(t,\mathbf{x},R)$, with $R \coloneqq R_1^2 + R_2^2$. Then, the first two terms in the definition of F obviously preserve rotational symmetry, i.e., $-\mathbf{u}\cdot\nabla_{\mathbf{x}}\phi(t,\mathbf{x},\mathbf{R}) = -\mathbf{u}\cdot\nabla_{\mathbf{x}}\hat{\phi}(t,\mathbf{x},R)$ and $\epsilon\Delta_{\mathbf{x}}\phi(t,\mathbf{x},\mathbf{R}) = \epsilon\Delta_{\mathbf{x}}\hat{\phi}(t,\mathbf{x},R)$, are also rotationally symmetric with respect to $\mathbf{R}$.

Since we are considering the corotational case, we can rewrite $\tau(\mathbf{u}) = \frac{1}{2}(\nabla_{\mathbf{x}}\mathbf{u} - (\nabla_{\mathbf{x}}\mathbf{u})^{\mathrm{T}})$ as

$$\tau(\mathbf{u}) = \frac{1}{2}(\partial_y\mathbf{u}_1 - \partial_x\mathbf{u}_2)\begin{pmatrix} 0 & 1 \\ -1 & 0 \end{pmatrix}. \tag{8}$$

Now, the third term in the definition of F equals zero, since

$$\nabla_{\mathbf{R}}\cdot(\tau(\mathbf{u})\mathbf{R}\phi) = \frac{1}{2}(\partial_y\mathbf{u}_1 - \partial_x\mathbf{u}_2)(\partial_{R_1}\hat{\phi}R_2 - \partial_{R_2}\hat{\phi}R_1) = (\partial_y\mathbf{u}_1 - \partial_x\mathbf{u}_2)\partial_R\hat{\phi}(R_1R_2 - R_1R_2) = 0. \tag{9}$$

It can be easily seen that also the fourth and fifth terms are rotationally symmetric. For the convenience of the reader, we provide the details. For the fourth term, we note that $\mathbf{R}\cdot\mathbf{R} = R$ and find that

$$\nabla_{\mathbf{R}}\cdot(\xi\mathbf{R}\phi) = 2\xi(\hat{\phi} + \partial_R\hat{\phi}R) \tag{10}$$

which is a function in R. Finally, the fifth term can be rewritten as

$$\chi\Delta_{\mathbf{R}}\phi = \chi\left(\nabla_{\mathbf{R}}\cdot\left(2\mathbf{R}\partial_R\hat{\phi}\right)\right) = \chi(4\partial_R^2\hat{\phi}R_1^2 + 4\partial_R^2\hat{\phi}R_2^2 + 4\partial_R\hat{\phi}) = 4\chi(R\partial_R^2\hat{\phi} + \partial_R\hat{\phi}). \tag{11}$$

Thus all terms in the definition of F preserve the rotational symmetry. Now, the result follows for a rotationally symmetric initial datum and the fact that $\partial_t\psi = F(\partial_t^{1-\alpha}\psi)$. □

2.2. Time-fractional Navier–Stokes–Fokker–Planck system

For the TFNSFP system, we consider a combination of Dirichlet and zero normal stress boundary conditions. Accordingly, we split the boundary of Ω as $\partial\Omega = \Gamma_D \cup \Gamma_N$, $\Gamma_D \cap \Gamma_N = \emptyset$. The boundary conditions for the Navier–Stokes system read as follows:

$$\mathbf{u} = \mathbf{u}_D, \quad \text{on } (0,T) \times \Gamma_D \times \mathcal{D}, \tag{12}$$

$$2\nu\nabla\mathbf{u} \cdot \mathbf{n} - p\mathbf{Id} \cdot \mathbf{n} = 0, \qquad \text{on } (0,T) \times \Gamma_N \times \mathcal{D}. \tag{13}$$

As was described in Section 2.1, for the solution, ψ, of the TFFPE we consider a homogeneous Neumann boundary condition on the boundary $\partial\Omega$ of the spatial domain Ω, see (7), in conjunction with sufficiently strong decay conditions as $|\mathbf{R}| \to \infty$.

As initial conditions, we set $\mathbf{u}(0) = \mathbf{u}^0$ and $\psi(0) = \psi^0$, where the choice of ψ^0 is discussed in Section 2.1. Generally, the choice of the initial condition for the TFFPE is a nontrivial question. For memory effects, the history of the material has to be considered from $-\infty$ to t. In the formulation of viscoelastic behavior using time-fractional derivatives this fact is compensated by the singularity of the integral kernel, thus allowing for nontrivial history despite the convolution integral ranging from 0 to t. The two ideas coincide, assuming that the viscoelastic material has been at rest from $t = -\infty$ until $t = 0$. The same question regarding the choice of the initial condition occurs in the theory of fractional viscoelasticity of solids, see, e.g., [49].

Again, we take a closer look at the corotational formulation of the TFFPE. As the additional stress tensor in the NSE is the spatial divergence of $\mathbf{T}$, we consider the case of an initial condition which is independent of $\mathbf{x}$.

Lemma 2. *Let $\tau(\mathbf{u}) = \frac{1}{2}(\nabla_{\mathbf{x}}\mathbf{u} - (\nabla_{\mathbf{x}}\mathbf{u})^{\mathrm{T}})$, and consider a natural boundary condition for the TFFPE on $\partial\Omega$. Suppose further that the initial datum ψ^0 is rotationally symmetric with respect to the conformation vector $\mathbf{R}$ and independent of the spatial variable $\mathbf{x}$. Then, the TFFPE has a solution ψ that is rotationally symmetric with respect to the conformation vector $\mathbf{R}$ and is independent of the spatial variable $\mathbf{x}$.*

Proof. Again, we provide the proof for the two-dimensional case; in the three-dimensional case the proof proceeds along the same lines. It is sufficient to show that for a sufficiently smooth $\phi(t, \mathbf{x}, \mathbf{R})$, which is rotationally symmetric in $\mathbf{R}$ and independent of $\mathbf{x}$, also $F(\phi)$ is such, where $F(\cdot)$ is defined in (1).

Let $\phi(t, \mathbf{x}, \mathbf{R}) = \hat{\phi}(t, R)$, with $R := R_1^2 + R_2^2$. Thanks to Lemma 1, $F(\phi)$ is rotationally symmetric and it remains to show that $F(\phi)$ is independent of $\mathbf{x}$. The first two terms in the definition of $F(\phi)$ vanish:

$$-\mathbf{u} \cdot \nabla_{\mathbf{x}}\phi(t, \mathbf{x}, \mathbf{R}) = -\mathbf{u} \cdot \nabla_{\mathbf{x}}\hat{\phi}(t, R) = 0, \quad \epsilon\Delta_{\mathbf{x}}\phi(t, \mathbf{x}, \mathbf{R}) = \epsilon\Delta_{\mathbf{x}}\hat{\phi}(t, R) = 0. \tag{14}$$

As previously shown in the proof of Lemma 1, thanks to the rotational symmetry of ϕ, $\nabla_{\mathbf{R}} \cdot (\tau(\mathbf{u})\mathbf{R}\phi) = 0$ as well. Finally, it is easy to see that the fourth and fifth terms are independent of $\mathbf{x}$:

$$\nabla_{\mathbf{R}} \cdot (\xi\mathbf{R}\phi(t, \mathbf{x}, \mathbf{R})) = \nabla_{\mathbf{R}} \cdot (\xi\mathbf{R}\hat{\phi}(t, R)), \quad \chi\Delta_{\mathbf{R}}\phi(t, \mathbf{x}, \mathbf{R}) = \chi\Delta_{\mathbf{R}}\phi(t, R). \tag{15}$$

Thus all terms in the definition of F preserve the independence from $\mathbf{x}$, and the result follows for a rotationally symmetric initial condition which is independent of $\mathbf{x}$ from the fact that $\partial_t \psi = F(\partial_t^{1-\alpha}\psi)$. □

The TFFPE is coupled to the Navier–Stokes system through the divergence of the Kramers stress tensor, $\mathbf{T}$, with respect to the spatial variable $\mathbf{x}$. In the setting of Lemma 2, the tensor $\mathbf{T}$ is independent of $\mathbf{x}$, and thus, the additional stress term vanishes and the TFNSFP system decouples. This demonstrates that the coupling in the corotational model is weaker than in the case of the general noncorotational model. In particular, in the corotational model the velocity field and the pressure can be calculated independently of ψ. First, we solve the NSE, and then, if we are also interested in the distribution of the polymer molecules ψ, the TFFPE is solved for the calculated velocity field, which is independent of ψ.

3. Algorithmic Components

Having stated the mathematical model under consideration, we now introduce the necessary fundamentals for the numerical scheme for the TFFPE, namely, weighted Hermite polynomials and a kernel compression method for the fractional integral based on rational approximation.

3.1. Hermite polynomials

We use a spectral method based on weighted Hermite polynomials to discretize the FPE over the configuration space $\mathcal{D} = \mathbb{R}^d$. We refer the interested reader to Chapter 7.2 in [50] for a more detailed introduction. The weighted Hermite polynomials are defined as follows:

$$\tilde{H}_m(r) \coloneqq \frac{e^{-a^2 r^2}}{\sqrt{2^m m!}} H_m(ar), \quad w_a(r) \coloneqq e^{a^2 r^2}, \quad a > 0, \quad r \in \mathbb{R}, \tag{16}$$

where $w_a(r)$ is the weight function, and H_m is the Hermite polynomial of degree m. For $r \in \mathbb{R}$, it is defined by $H_m(r) \coloneqq (-1)^m e^{r^2} \partial_r^m (e^{-r^2})$. Over a bounded interval the approximation properties of unscaled Hermite polynomials corresponding to $a = 1$ are poor [51]. This can be improved upon by the introduction of the parameter a; for example, the standard Gaussian weight corresponds to $a = \frac{1}{\sqrt{2}}$, [27]; see also [52] for numerical results for different values of a. In this work we take $a = \frac{1}{2}$.

In order to derive a numerical scheme for equation (2), we will use the following well-known properties of the weighted Hermite polynomials.

Theorem 3 (Properties of weighted Hermite polynomials)**.**

1. *Weighted Hermite polynomials are orthogonal with respect to the weight w_a function, i.e.,*

$$\int_{\mathbb{R}} \tilde{H}_m(r) \tilde{H}_n(r) w_a(r) dr = \frac{\sqrt{\pi}}{a} \delta_{mn}. \tag{17}$$

2. *For $m \geq 1$, weighted Hermite polynomials satisfy*

$$\int_{\mathbb{R}} \tilde{H}_m(r) dr = 0. \tag{18}$$

3. For weighted Hermite polynomials, one has

$$\lim_{r\to\infty} \tilde{H}_m(r) = 0. \tag{19}$$

4. Weighted Hermite polynomials satisfy the following identities:

$$ar\tilde{H}_m(r) = \sqrt{\frac{m+1}{2}}\tilde{H}_{m+1}(r) + \sqrt{\frac{m}{2}}\tilde{H}_{m-1}(r), \tag{20}$$

$$\frac{\partial \tilde{H}_m(r)}{\partial r} = -a\sqrt{2(m+1)}\tilde{H}_{m+1}(r), \tag{21}$$

$$r\frac{\partial \tilde{H}_m(r)}{\partial r} = -\sqrt{(m+1)(m+2)}\tilde{H}_{m+2}(r) - (m+1)\tilde{H}_m(r), \tag{22}$$

$$\frac{\partial^2 \tilde{H}_m(r)}{\partial r \partial r} = 2a^2\sqrt{(m+1)(m+2)}\tilde{H}_{m+2}(r). \tag{23}$$

For proofs of these assertions we refer the reader to [27, 50]. We use a spectral method based on such weighted Hermite polynomials, i.e., we seek an approximation ψ_N of ψ of the form

$$\psi_N(t,\mathbf{x},\mathbf{R}) = \sum_{i_1,\dots,i_d=0}^{N} \phi_{i_1,\dots,i_d}(t,\mathbf{x}) \prod_{l=1}^{d} \tilde{H}_{i_l}(R_l). \tag{24}$$

We introduce the notation $\phi[\psi] = (\phi_{0,\dots,0},\dots,\phi_{N,\dots,N})$ for the $(N+1)^d$-dimensional vector containing all $\phi_{i_1,\dots,i_d}$ of the approximation of ψ. Note that such an approximation with weighted Hermite polynomials inherently decays exponentially as $|\mathbf{R}| \to \infty$. Further, thanks to equation (18), we obtain

$$\int_{\mathcal{D}} \psi_N(t,\mathbf{x},\mathbf{R})d\mathbf{R} = \sum_{i_1,\dots,i_d=0}^{N} \phi_{i_1,\dots,i_d}(t,\mathbf{x}) \int_{\mathcal{D}} \prod_{l=1}^{d} \tilde{H}_{i_l}(R_l)d\mathbf{R} = \phi_{0,\dots,0}(t,\mathbf{x}) \left(2\sqrt{\pi}\right)^d, \tag{25}$$

and thus the polymer number density $\int_{\mathcal{D}} \psi(t,\mathbf{x},\mathbf{R})d\mathbf{R}$ is approximated by $\phi_{0,\dots,0}(t,\mathbf{x})\left(2\sqrt{\pi}\right)^d$.

3.2. Rational approximation

We use a kernel compression method based on rational approximation [53] to discretize the time-fractional derivative. The integral kernel is approximated by a sum of exponentials and a singular term. First, we show how such an approximation can be used to transform the nonlocal-in-time TFFPE into a system of ordinary differential equations, which is ameanable to approximate the solution by standard numerical methods for ODEs. We then address the question of computing the approximation of the integral kernel. The approximation K_α of the fractional integral kernel K_α reads as follows:

$$\tilde{K}_\alpha(t) \coloneqq \sum_{k=1}^{m} w_k e^{-\lambda_k t} + w_\infty \delta(t), \tag{26}$$

where $\delta(t)$ denotes the Dirac-distribution concentrated at $t = 0$. Note that by Bernstein's theorem for completely monotone functions [54] applied to the special case of exponential sums, the approximate kernel $\tilde{K}_\alpha$ is completely monotone if the weights w_k and the poles λ_k are nonnegative for all $k = 1,\dots,m$. Replacing K_α with $\tilde{K}_\alpha$ in the TFFPE, we obtain

$$\partial_t \psi = F\left(\partial_t \tilde{K}_\alpha * \psi\right) = F\left(\partial_t\left(\sum_{k=1}^{m}\int_0^T w_k e^{-\lambda_k(t-s)}\psi(s)ds + w_\infty\psi(t)\right)\right). \tag{27}$$

Note that the integrals in the sum correspond to the solution formula for ordinary differential equations. We define the modes ψ_k and ψ_∞ as follows:

$$\psi_k(t) = w_k \int_0^t e^{-\lambda_k(t-s)}\psi(s)ds, \quad k = 1, \dots, m, \tag{28}$$

$$\psi_\infty(t) = w_\infty \psi(t). \tag{29}$$

Now, for $k \in \{1, \dots, m\}$, the mode ψ_k is the solution of the ODE initial-value problem

$$\partial_t \psi_k + \lambda_k \psi_k - w_k \psi = 0, \tag{30}$$

$$\psi_k(0) = 0. \tag{31}$$

To preserve $(K_\alpha * \psi)(0) = 0$, we also set $\psi_\infty(0) = 0$ resulting in a discontinuity at $t = 0$ for ψ_∞. After exploiting the kernel compression technique, the approximate version of the TFFPE reads as follows:

$$\partial_t \psi = F\left(\partial_t\left(\sum_{k=1}^{m} \psi_k + \psi_\infty\right)\right). \tag{32}$$

The nonlocal in time TFFPE has thus been transformed into a system of ordinary differential equations, whereby the history effects of the convolution are stored in the modes. The new system can be solved using standard numerical methods. In the case of $\alpha = 1$ the weights are set to $w_1 = 1$ and $w_k = 0$ for $k \neq 1$, and the poles are set to $\lambda_k = 0$ for all k.

It remains to obtain an approximation of the integral kernel K_α. To this end, we follow the ideas of Khristenko and Wohlmuth [53]. We consider the Laplace transform $\mathcal{L}\{K_\alpha\}$ of the integral kernel and approximate it by a rational function. The rational approximation is obtained by appying the AAA-algorithm [55] to the inverse Laplace transform of $\mathcal{L}\{K_\alpha\}$; we refer the interested reader to [53] for the details. We calculate the partial fraction decomposition of the rational approximation and apply the inverse Laplace transform. This results in a sum of exponentials and a singular term as shown in equation (26).

While there is no mathematical proof, we observe numerically that for $0 < \alpha < 1$ the weights w_k and poles λ_k, $k = 1, \dots, m$, are all positive. The required number of modes m depends on the value of α, the tolerance used for the AAA-algorithm, and the interval considered for the rational approximation. Since m is fixed, the required memory and the computational complexity remain constant, while, generally, the number of modes and the required storage grow logarithmically with the number of time steps [53].

4. Solving the Time-fractional Fokker–Planck Equation

After laying the necessary foundations, this section focuses on the numerical method for solving the TFFPE. We discretize the time-fractional derivative in time, apply a space-splitting approach, and solve the problems over the configuration space $\mathcal{D} = \mathbb{R}^d$ and the physical domain Ω separately using a Hermite spectral method over $\mathcal{D}$ and an $H^1(\Omega)$ conforming finite element method over Ω.

4.1. Kernel compression and space-splitting - time

We discretize equation (2) in time, using a first-order implicit time discretization. Note that, together with the space-splitting, which is inherently a first-order Strang splitting, this is the limiting factor for the order of the complete method. This could be improved upon by utilizing a higher-order time integration scheme in combination with a symmetric operator splitting scheme. We divide the interval $[0, T]$ into N_T subintervals of equal length $\Delta t = T/N_T$ and obtain

$$\psi^{n+1} = \psi^n + F(K_\alpha * \psi)(t^{n+1}) - F(K_\alpha * \psi)(t^n). \tag{33}$$

For the first time step $n = 0$, we exploit that $F(K_\alpha * \psi)(0) = 0$ thanks to the definition of the convolution, assuming that the solution has suitable regularity at $t = 0$. By inserting the approximation $\tilde{K}_\alpha$ into equation (2) and using the definitions (28) and (29) of the modes results in

$$\psi^{n+1} = \psi^n + F\left(\sum_{k=1}^{m} \psi_k^{n+1} + w_\infty \psi^{n+1}\right) - F\left(\sum_{k=1}^{m} \psi_k^{n} + w_\infty \psi^{n}\right). \tag{34}$$

To handle the term ψ_k^{n+1}, $k = 1, \dots m$, we discretize the mode equation in time. Again, we apply the implicit Euler method and find

$$\psi_k^{n+1} = \psi_k^n - \Delta t \lambda_k \psi_k^{n+1} + \Delta t w_k \psi^{n+1} = \gamma_k \left(\psi_k^n + \Delta t w_k \psi^{n+1}\right), \tag{35}$$

where γ_k is defined as $(1 + \Delta t \lambda_k)^{-1}$. We substitute ψ_k^{n+1} in equation (34) and obtain

$$\psi^{n+1} - \beta F\left(\psi^{n+1}\right) = \psi^n + F\left(\sum_{k=1}^{m} (\gamma_k - 1)\psi_k^n - w_\infty \psi^n\right), \tag{36}$$

where $\beta = \sum_{k=1}^{m} \Delta t \gamma_k w_k + w_\infty$. After solving for ψ^{n+1}, we can calculate ψ_k^{n+1} with the linear update in equation (35).

Now, we apply a first-order Strang splitting [56], see also [57], to equation (36) to separate the problem into its configuration space part and its physical space part. This space-splitting approach has previously been applied to the NSFP system in [25, 58]. We introduce two operators $F_{\mathbf{R}}$ and $F_{\mathbf{x}}$ such that $F = F_{\mathbf{R}} + F_{\mathbf{x}}$. $F_{\mathbf{R}}$ consists of all terms of F which contain derivatives with respect to the configuration space variable $\mathbf{R}$ and all terms with spatial derivatives are collected in $F_{\mathbf{x}}$. The two operators read as follows

$$F_{\mathbf{R}}(\psi) \coloneqq -\nabla_R \cdot (\tau(\mathbf{u}) \cdot \mathbf{R}\psi) + \nabla_R \cdot (\xi \mathbf{R}\psi) + \chi \Delta_R \psi, \tag{37}$$

$$F_{\mathbf{x}}(\psi) \coloneqq -\mathbf{u} \cdot \nabla_x \psi + \epsilon \Delta_x \psi. \tag{38}$$

For the space-splitting approach, we split equation (36) into two equations, which are solved separately. First, we fix a point $\mathbf{x} \in \Omega$ in the physical domain and solve the problem with respect to the configuration space:

$$\psi^{n+\frac{1}{2}} - \beta F_{\mathbf{R}}\left(\psi^{n+\frac{1}{2}}\right) = \psi^n + F_{\mathbf{R}}\left(\sum_{k=1}^{m} (\gamma_k - 1)\psi_k^n - w_\infty \psi^n\right), \tag{39}$$

to obtain an intermediate solution $\psi^{n+\frac{1}{2}}$ at that point $\mathbf{x}$. By interpreting $\mathbf{x}$ as a 'meshpoint' in $\overline{\Omega}$, these computations can be performed in parallel for all meshpoints in $\overline{\Omega}$ as they are mutually independent. We then fix a point $\mathbf{R} \in \mathcal{D}$ in the configuration space and solve the problem in the physical domain

$$\psi^{n+1} - \beta F_{\mathbf{x}}\left(\psi^{n+1}\right) = \psi^{n+\frac{1}{2}} + F_{\mathbf{x}}\left(\sum_{k=1}^{m}(\gamma_k - 1)\psi_k^{n+\frac{1}{2}} - w_\infty \psi^{n+\frac{1}{2}}\right). \tag{40}$$

By interpreting $\mathbf{R}$ now as a 'meshpoint' in the configuration space domain, and noting that, again, these computations can be performed in parallel as they are mutually independent, we obtain the full numerical approximation ψ^{n+1} to ψ at timestep $(n+1)$.

4.2. Hermite spectral method - configuration space

We approximate the solution of equation (39) using the Hermite spectral method outlined in [12]. Further details regarding spectral methods can be found in [50, 59] and the references therein. We use equation (24) to approximate ψ and ψ_k with sums of weighted Hermite polynomials ψ_N and $\psi_{N,k}$. The corresponding ϕ are denoted with $\phi[\psi]$ and $\phi[\psi_k]$, respectively. Thus, we consider the following equation

$$\psi_N^{n+\frac{1}{2}} - \beta F_{\mathbf{R}}\left(\psi_N^{n+\frac{1}{2}}\right) = \psi_N^n + F_{\mathbf{R}}\left(\sum_{k=1}^{m}(\gamma_k - 1)\psi_{N,k}^n - w_\infty \psi_N^n\right). \tag{41}$$

We multiply equation (41) with the test function $\prod_{l=1}^{d}\tilde{H}_{z_l}(R_l)w_a(R_l)$ and integrate over the configuration space. As an illustration, we consider an arbitrary approximation η_N of a function η. Using the orthogonality of the weighted Hermite polynomials stated in Theorem 3.1, we obtain

$$\int_{\mathcal{D}} \eta_N \prod_{l=1}^{d}\tilde{H}_{z_l}(R_l)w_a(R_l)d\mathbf{R} = \sum_{i_1,\ldots,i_d=0}^{N}\phi[\eta]_{i_1,\ldots,i_d}(t,\mathbf{x})\int_{\mathcal{D}}\prod_{l=1}^{d}\tilde{H}_{i_l}(R_l)\prod_{l=1}^{d}\tilde{H}_{z_l}(R_l)w_a(R_l)d\mathbf{R} \tag{42}$$

$$= \phi[\eta]_{z_1,\ldots,z_d}(t,\mathbf{x})\left(\frac{\sqrt{\pi}}{a}\right)^d. \tag{43}$$

We proceed analogously for $F_{\mathbf{R}}(\eta_N)$. Since $\phi[\eta]_{i_1,\ldots,i_d}$ depends only on t and $\mathbf{x}$, we can pull it out of the integral over $\mathcal{D}$. Thus, we apply the operators with respect to $\mathbf{R}$ directly to the product of weighted Hermite polynomials. We apply Theorem 3.4 to rewrite the derivatives of the weighted Hermite polynomials in terms of weighted Hermite polynomials of a different degree. Again, exploiting the orthogonality, we obtain

$$\int_{\mathcal{D}} F_{\mathbf{R}}(\eta_N)\prod_{l=1}^{d}\tilde{H}_{z_l}(R_l)w_a(R_l)d\mathbf{R} = \sum_{i_1,\ldots,i_d=0}^{N}\phi[\eta]_{i_1,\ldots,i_d}(t,\mathbf{x})\int_{\mathcal{D}}F_{\mathbf{R}}\left(\prod_{l=1}^{d}\tilde{H}_{i_l}(R_l)\right)\prod_{l=1}^{d}\tilde{H}_{z_l}(R_l)w_a(R_l)d\mathbf{R} \tag{44}$$

$$= A(\phi[\eta])_{z_1,\ldots,z_d}\left(\frac{\sqrt{\pi}}{a}\right)^d,$$

where A is defined by

$$A(\phi)_{z_1,\dots,z_d} \coloneqq \phi_{z_1,\dots,z_d} \sum_{l=1}^{d} \left(\tau(\mathbf{u})_{ll} - \xi\right) z_l + \sum_{l=1}^{d} \phi_{(z_l-2)} \left(2a^2\chi + \tau(\mathbf{u})_{ll} - \xi\right) \sqrt{(z_l-1)z_l} \tag{45}$$
$$+ \sum_{1\le l\neq m\le d} \phi_{(z_l+1,z_m-1)} \tau(\mathbf{u})_{ml} \sqrt{(z_l+1)z_m} + \sum_{1\le l\neq m\le d} \phi_{(z_l-1,z_m-1)} \tau(\mathbf{u})_{ml} \sqrt{z_l z_m}.$$

In equation (45), we have used the notation $(z_l - 2)$ to indicate that the index z_l is replaced with $z_l - 2$, while all other indices remain unchanged. Similarly, $(z_m + 1, z_l - 1)$ indicates that the indices z_m and z_l are replaced with $z_m + 1$ and $z_l - 1$, respectively. If one of the new indices is less than zero or larger than N, we set the value of the corresponding $\phi_{z_1,\dots,z_d}$ to zero. Combining equations (42) and (44) results in

$$\phi[\psi^{n+\frac{1}{2}}] - \beta A(\phi[\psi^{n+\frac{1}{2}}]) = \phi[\psi^n] + A\left(\sum_{k=1}^{m} (\gamma_k - 1)\phi[\psi_k^n] - w_\infty \phi[\psi^n]\right). \tag{46}$$

By using the Hermite spectral method, the problem with respect to the configuration space is transformed into a system of $(N+1)^d$ linear ordinary differential equations that has to be solved for every point $\mathbf{x} \in \Omega$. Note that since $A(\phi_{0,\dots,0}) = 0$, the operator A preserves $\phi_{0,\dots,0}$.

Analogously, we proceed with the update rules of the modes. We multiply the equality (46) by the test function $\prod_{l=1}^{d} \tilde{H}_{z_l}(R_l) w_a(R_l)$ and integrate over the configuration space. Consequently, for $k \in \{1, \dots, m\}$ and $z_1, \dots, z_d \in \{0, \dots, N\}$, we obtain

$$\phi[\psi_k^{n+\frac{1}{2}}] = \gamma_k \left(\phi[\psi_k^n] + \Delta t w_k \phi[\psi^{n+\frac{1}{2}}]\right). \tag{47}$$

4.3. Finite element method - physical space

Before applying the finite element method to the physical space problem we reformulate the problem in terms of the Hermite spectral method. Again, we approximate ψ and ψ_k with ψ_N and $\psi_{N,k}$, respectively, as shown in equation (24). Thus, the physical space problem reads as follows:

$$\psi_N^{n+1} - \beta F_{\mathbf{x}}\left(\psi_N^{n+1}\right) = \psi_N^{n+\frac{1}{2}} + F_{\mathbf{x}}\left(\sum_{k=1}^{m} (\gamma_k - 1)\psi_{N,k}^{n+\frac{1}{2}} - w_\infty \psi_N^{n+\frac{1}{2}}\right). \tag{48}$$

Next, we multiply the equation by the test function $\prod_{l=1}^{d} \tilde{H}_{z_l}(r_l) w_a(r_l)$, $z_1, \dots, z_d \in \{0, \dots, N\}$, and integrate over the configuration space $\mathcal{D}$. Since the operator $F_{\mathbf{x}}$ only contains terms involving derivatives with respect to the physical domain, we obtain

$$\phi[\psi^{n+1}] - \beta F_{\mathbf{x}}\left(\phi[\psi^{n+1}]\right) = \phi[\psi^{n+\frac{1}{2}}] + F_{\mathbf{x}}\left(\sum_{k=1}^{m} (\gamma_k - 1)\phi[\psi_k^{n+\frac{1}{2}}] - w_\infty \phi[\psi^{n+\frac{1}{2}}]\right), \tag{49}$$

which is a standard advection-diffusion equation for each entry of ϕ. As shown above, we derive the mode update

$$\phi[\psi_k^{n+1}] = \gamma_k \left(\phi[\psi_k^{n+\frac{1}{2}}] + \Delta t w_k \phi[\psi^{n+1}]\right). \tag{50}$$

Finally, we discretize the problem in the physical space using a standard $H^1(\Omega)$-conforming Galerkin finite element method and adapt the operator $F_{\mathbf{x}}$ according to the boundary conditions. For later use, we introduce the notation here. Let Ω be a polygonal domain ($d = 2$) or a polyhedral Lipschitz domain ($d = 3$), consider a family of triangulations $\{\mathcal{T}_h\}_{h\in\mathcal{H}}$ of $\overline{\Omega}$ with vertex-set $\{\Omega_h\}_{h\in\mathcal{H}}$, where h denotes the maximal overall diameter of elements in the triangulation, and we denote the associated family of finite element spaces by $\{\mathcal{X}_h\}_{h\in\mathcal{H}}$.

4.4. Algorithm for solving the TFFPE

Finally, we combine the previously described numerical methods and state the full algorithm for the TFFPE. The algorithm is formulated in terms the spectral modes, i.e., $\phi[\cdot]$. Following the finite element discretization of the problem over the spatial domain Ω, $\phi[\cdot]$ is an $(N+1)^d$-dimensional vector with entries in $\mathcal{X}_h$.

Let the initial condition ψ^0, in the form $\phi[\psi^0]$, the values of the velocity field $\mathbf{u}^n$ at all time steps $n \in \{0,\dots,N_T\}$, and the weights w_k and the poles λ_k of the rational approximation be given. For the computation of the intermediate step $n+\frac{1}{2}$ and the full time step $n+1$, we consider the operator F depending on $\mathbf{u}^{n+1}$. For $k \in \{1,\dots,m\}$, we set $\phi[\psi_k^0] = 0$.

For every time step $t^{n+1} = (n+1)\Delta t$, $n \in \{0,\dots,N_T-1\}$, we carry out the following calculations:

Step 1: For $\mathbf{x} \in \Omega_h$, we solve the algebraic equation

$$\phi[\psi^{n+\frac{1}{2}}] - \beta A(\phi[\psi^{n+\frac{1}{2}}]) = \phi[\psi^n] + A\left(\sum_{k=1}^{m}(\gamma_k - 1)\phi[\psi_k^n] - w_\infty\phi[\psi^n]\right). \tag{51}$$

Step 2: For every entry of ϕ, we solve the partial differential equation

$$\phi[\psi^{n+1}] - \beta F_{\mathbf{x}}\left(\phi[\psi^{n+1}]\right) = \phi[\psi^{n+\frac{1}{2}}] + F_{\mathbf{x}}\left(\sum_{k=1}^{m}(\gamma_k - 1)\phi[\psi_k^{n+\frac{1}{2}}] - w_\infty\phi[\psi^{n+\frac{1}{2}}]\right). \tag{52}$$

Step 3: We update the modes for the full time step. For $k \in \{1,\dots,m\}$

$$\phi[\psi_k^{n+1}] = \phi[\psi_k^{n+\frac{1}{2}}] + \Delta t w_k \phi[\psi^{n+1}]. \tag{53}$$

We can carry out Step 1 efficiently by exploiting the structure of the operator A in (45). For ease of readability, we restrict ourselves to the case $d = 2$. In matrix/vector notation, we obtain a problem of the form

$$\Phi - \mathbf{B}\Phi = \mathbf{b}, \tag{54}$$

where Φ, $\mathbf{B}$, and $\mathbf{b}$, represent $\phi[\psi^{n+\frac{1}{2}}]$, βA, and the right-hand side of equation (46) written using matrix/vector notation. Thanks to the structure of A, every entry of Φ is dependent on at most 6 entries, namely, $\phi_{i,j}$ depends on $\phi_{i,j}$, $\phi_{i-1,j-1}$, $\phi_{i+1,j-1}$, $\phi_{i-1,j+1}$, $\phi_{i-2,j}$, and $\phi_{i,j-2}$. The dependency structure of $\phi_{i,j}$ is visualized in Figure 1. Also, if $i+j$ is an even (odd) number, then $\phi_{i,j}$ only depends on ϕ whose indices

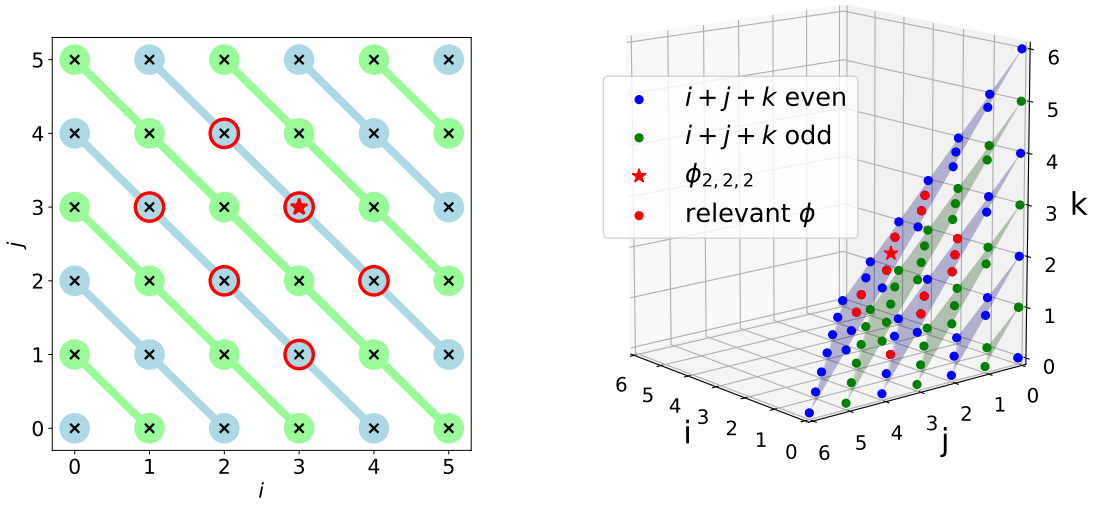

(a) Two-dimensional case

(b) Three-dimensional case

Figure 1: Dependency structure of ϕ in two [three] dimensions. The blue and green colors highlight the $\phi_{i,j}$ [$\phi_{i,j,k}$], where $i+j$ [$i+j+k$] is an even or odd number. A red star marks $\phi_{3,3}$ [$\phi_{2,2,2}$]. All relevant ϕ for its computation are highlighted in red.

add up to an even (odd) number. Therefore, we can rewrite equation (54) in the form of block matrices:

$$\begin{pmatrix} \Phi_{even} \\ \Phi_{odd} \end{pmatrix} = \begin{pmatrix} \mathbf{b}_1 \\ \mathbf{b}_2 \end{pmatrix} + \begin{pmatrix} \mathbf{B}_{even} & 0 \\ 0 & \mathbf{B}_{odd} \end{pmatrix} \begin{pmatrix} \Phi_{even} \\ \Phi_{odd} \end{pmatrix}. \tag{55}$$

We point out that in a physical relevant setting the initial datum has to satisfy $\psi^0(\mathbf{x}, \mathbf{R}) = \psi^0(\mathbf{x}, -\mathbf{R})$ and thus the odd block part of the system does not have to be solved as all its component are equal to zero for all time steps.

Further, we observe that if the indices of $\phi_{i,j}$ sum up to k, then it only depends on ϕ whose indices sum up to k or to $k-2$. Therefore, $\mathbf{B}_{even}$ and $\mathbf{B}_{odd}$ can be rewritten as block lower tridiagonal matrices:

$$\mathbf{B}_{even} = \begin{pmatrix} B_{0,0} & 0 & 0 & 0 \\ B_{2,0} & B_{2,2} & 0 & 0 \\ 0 & B_{4,2} & B_{4,4} & 0 \\ 0 & 0 & \ddots & \ddots \end{pmatrix}, \quad \mathbf{B}_{odd} = \begin{pmatrix} B_{1,1} & 0 & 0 & 0 \\ B_{3,1} & B_{3,3} & 0 & 0 \\ 0 & B_{5,3} & B_{5,5} & 0 \\ 0 & 0 & \ddots & \ddots \end{pmatrix}, \tag{56}$$

where $B_{k,l}$ describes the dependencies of all ϕ whose indices add up to k on all ϕ whose indices add up to l. Due to this algebraic structure, equation (54) can be solved extremely efficiently using forward substitution on block matrices. Also, recall that both $\mathbf{B}_{even}$ and $\mathbf{B}_{odd}$ are sparse, with at most 6 entries in each row.

Finally, we consider the cost of the algorithm. For one time step, solving the inherently $2d$-dimensional Fokker–Planck system requires solving ${N_h}^d$ systems of linear ordinary differential equations of size $(N+1)^d$ and solving $(N+1)^d$ partial differential equations. Exploiting the structure of the first step of the algorithm

results in solving $\mathcal{O}(N{N_h}^d)$ systems of linear ordinary differential equations of size $\mathcal{O}(N^{d-1})$.

Note that the m the parameter from the approximation of the integral kernel does not occur above. Its relevance is restricted to the update of the modes and the accumulation of the right-hand side. Therefore, we choose m sufficiently large. Nevertheless, the required storage grows linearly in m, as for every mode a vector of the same size as the solution is stored.

Further note that the algorithm described above is well-suited for parallelization. Both the first and second step can be easily distributed to multiple processors. For every $\mathbf{x} \in \Omega_h$, the problem in the configuration space can be solved on a separate processor. Also, the advection-diffusion equations are solved for every spectral mode separately, and thus, can be distributed to $(N+1)^d$ processing units.

5. Solving the Time-fractional Navier–Stokes–Fokker–Planck Equation

This section concerns solving the NSE and the coupling between the TFFPE and the NSE. The Navier–Stokes solver is based on the projection method originally presented by Chorin [60, 61]. We refer the interested reader to the review article by Guermond et al. [62] for an overview of different variants of the technique. In this work, we follow the variant outlined in [63], which was first described in [64]. Explicit descriptions of the spatial discretization can be found in Chapter 3 of [63], and the projection method for the time integration is outlined in Chapter 4.2 of [63].

In summary, to compute $\mathbf{u}^{n+1}$, we first introduce time-extrapolated versions of the linear and nonlinear terms in the NSE. Considering the divergence of the resulting equation, we obtain a Poisson-type problem that can be solved for the pressure p^{n+1}. Reintroducing the pressure in the NSE, we solve a Helmholtz-type problem for $\mathbf{u}^{n+1}$. A matrix-free version of this solver is available as part of the MFEM library, including exhaustive benchmark settings. We use an implicit-explicit coupling between the two solvers, i.e., we calculate the velocity field $\mathbf{u}^{n+1}$ for the coupling tensor $\mathbf{T}^n$, which depends on the solution ψ and modes ψ_k of previous time steps. Afterwards, we solve the TFFPE for ψ^{n+1} depending on the velocity $\mathbf{u}^{n+1}$.

The solution of the TFFPE enters into the NSE, in general, in the form of the Kramers stress tensor $\mathbf{T}$, which depends on the time-fractional derivative of ψ. For $\mathbf{C}(\partial_t^{1-\alpha}\psi)$, we use the same time discretization as for $F(\partial_t^{1-\alpha}\psi)$, see equation (34):

$$\mathbf{C}(\partial_t^{1-\alpha})(t^n) = \frac{1}{\Delta t}\left(\mathbf{C}(K_\alpha * \psi)(t^n) - \mathbf{C}(K_\alpha * \psi)(t^{n-1})\right). \tag{57}$$

To determine the velocity $\mathbf{u}^1$, we set $\mathbf{C} = 0$. For $n = 1$, the second term on the right-hand side is zero as $(K_\alpha * \psi)(0) = 0$, assuming suitable regularity of the solution ψ at $t = 0$. For ease of readability, we continue with the non-discretized notation of the time-fractional derivative.

Inserting equation (24) into the definition of $\mathbf{C}$, we obtain for its numerical approximation

$$\mathbf{C}_N = \int_{\mathbb{R}^d} \partial_t^{1-\alpha}\psi_N(t,\mathbf{x},\mathbf{R})\mathbf{R}\mathbf{R}^T d\mathbf{R} = \sum_{i_1,\dots,i_d=0}^{N} \partial_t^{1-\alpha}\phi[\psi]_{i_1,\dots,i_d}(t,\mathbf{x}) \int_{\mathbb{R}^d} \mathbf{R}\mathbf{R}^T \prod_{l=1}^{d} \tilde{H}_{i_l}(r_l) d\mathbf{R}, \tag{58}$$

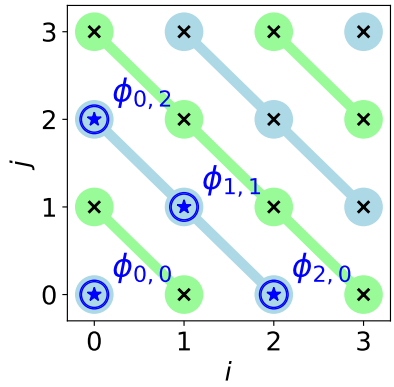

Figure 2: Sketch of the dependencies of $\phi_{0,0}$, $\phi_{0,2}$, $\phi_{1,1}$, and $\phi_{2,0}$. All $\phi_{i,j}$ relevant for their computation are highlighted with blue stars.

where the integrals can be evaluated analytically. Since $\int_{\mathbb{R}} r\tilde{H}_m(r)dr = 0$ for $m \neq 1$ and $\int_{\mathbb{R}} r^2\tilde{H}_m(r)dr = 0$ for $m \notin \{0, 2\}$, we can rewrite equation (58) as

$$\mathbf{C}_N = \sum_{0 \leq \sum_{l=1}^{d} i_l \leq 2} \partial_t^{1-\alpha} \phi[\psi]_{i_1,\ldots,i_d} \int_{\mathbb{R}^d} \mathbf{R}\mathbf{R}^T \prod_{l=1}^{d} \tilde{H}_{i_l}(r_l) d\mathbf{R}. \tag{59}$$

For $d = 2$, we obtain

$$\mathbf{C}_N = \partial_t^{1-\alpha} \left(\phi[\psi]_{0,0} \begin{pmatrix} c_{0,0} & 0 \\ 0 & c_{0,0} \end{pmatrix} + \phi[\psi]_{0,2} \begin{pmatrix} 0 & 0 \\ 0 & c_{0,2} \end{pmatrix} + \phi[\psi]_{1,1} \begin{pmatrix} 0 & c_{1,1} \\ c_{1,1} & 0 \end{pmatrix} + \phi[\psi]_{2,0} \begin{pmatrix} c_{2,0} & 0 \\ 0 & 0 \end{pmatrix} \right), \tag{60}$$

where $c_{0,0}, c_{0,2}, c_{1,1}, c_{2,0} \in \mathbb{R}$ are the values of the analytically evaluated integrals.

In our numerical scheme for the TFFPE, we know from the definition of the operator A in equation (45), that in 2D (3D) each $\phi_{i,j}$ is dependent on at most 6 (13) other $\phi_{i,j}$. The dependencies of $\phi_{0,0}$, $\phi_{0,2}$, $\phi_{1,1}$, and $\phi_{2,0}$ are visualized in Figure 2. Since all $\phi_{i,j}$ with negative indices are considered as 0, it becomes apparent that $\phi_{0,0}$, $\phi_{0,2}$, $\phi_{1,1}$, and $\phi_{2,0}$ depend only on themselves. Therefore, $N = 2$ is sufficient to compute the considered coupling term. Thus, instead of solving the 4-dimensional (6-dimensional) FP system, it is sufficient to solve a coupled 2-dimensional (3-dimensional) system with 4 (7) components. Our approach can easily be generalized to other coupling terms besides Kramers' expression.

6. Numerical Results

In this section, we provide further details about implementing the numerical method and present numerical results for the TFFPE and the TFNSFP system. We validate our solver for the TFFPE with an analytical solution, show the influence of the order α of the time-fractional derivative, compare the general noncorotational and corotational formulations of the drag term, and explore the influence of the polynomial degree in the Hermite spectral method.

6.1. Implementation

The numerical method presented above can be easily implemented within any modern finite element framework. We use MFEM [65], a state-of-the-art, open-source C++ library for finite element methods. The entire code, including the setting of our numerical experiments, is available on GitHub[1].

Following [53], we use the AAA-algorithm [55] to calculate the weights and the poles in the rational approximation technique employed. To achieve a fixed number of modes m, we consider a fixed interval $[\Delta t, T]$ and vary the tolerance of the AAA-algorithm to obtain a given number of modes. Since, for our approach, the weights and poles do not change throughout the simulation, we precompute the rational approximation before the simulation. While no theoretical result ensures that the resulting weights and poles are positive, this is the case for all scenarios studied computationally in this paper.

6.2. Simulation of the time-fractional Fokker-Planck equation

We present numerical results for the TFFPE. We verify our method against an analytical solution, study the convergence behavior of the method, and investigate the difference between the corotational and the general noncortational drag terms.

6.2.1. Comparison with an analytical solution

For the construction of an analytical solution we set the velocity field $\mathbf{u} = \mathbf{0}$, assume that the parameters χ, ξ and ϵ are constant, and thus, the operator F is independent of t. We consider an initial datum of the form $\psi_0 = \sum_{i=1}^n v_i$, where v_i are eigenfunctions of the operator F with eigenvalues θ_i. Then, the solution of

$$\partial_t \psi = F(\partial_t^{1-\alpha}\psi), \quad \psi(0, \mathbf{x}, \mathbf{R}) = \sum_{i=1}^n v_i(\mathbf{x}, \mathbf{R}), \tag{61}$$

is given by $\psi(t, \mathbf{x}, \mathbf{R}) = \sum_{i=1}^n v_i(\mathbf{x}, \mathbf{R}) E_\alpha(\theta_i t^\alpha)$, where E_α denotes the single-valued Mittag–Leffler function, see, e.g., [32]. For the simulations we set $\xi = \chi = 1, \epsilon = 0.01$, and chose the initial datum

$$\psi_0(\mathbf{x}, \mathbf{R}) = c e^{-\frac{|\mathbf{R}|^2}{2}} \left(1 + R_1 R_2 + \cos(2\pi x_1)\cos(4\pi x_2) + \cos(2\pi x_1)\cos(4\pi x_2) R_1 R_2\right), \tag{62}$$

where $\mathbf{R} = (R_1, R_2)$ with $R_1, R_2 \in \mathbb{R}$, c is a normalizing factor, and the four summands are eigenfunctions of F with eigenvalues $\theta_1 = 0$, $\theta_2 = -2$, $\theta_3 = -0.2\pi^2$, $\theta_4 = -2 - 0.2\pi^2$. Note that this initial datum is not physically meaningful as it isn't nonnegative. However, it satisfies $\psi_0(\mathbf{x}, \mathbf{R}) = \psi_0(\mathbf{x}, -\mathbf{R})$ and thus the system for the odd components in (55) does not have to be solved as they are equal to zero.

For the simulation, we consider $\alpha = 0.2, 0.5, 0.8$ and set $\Delta t = 0.001$, $N = 20$, $\Delta x = 0.1$. The solution ψ over the configuration space and ψ_0 over the spatial domain at $t = 0.01$ are displayed in Figure 3. We compare our numerical results with the analytical solution in Figure 4. In Figure 4a, we observe that the difference between the numerical results and the analytical solution is the largest in the beginning and decreases over

[1] `https://github.com/JonasBeddrich/TFNSFPE`

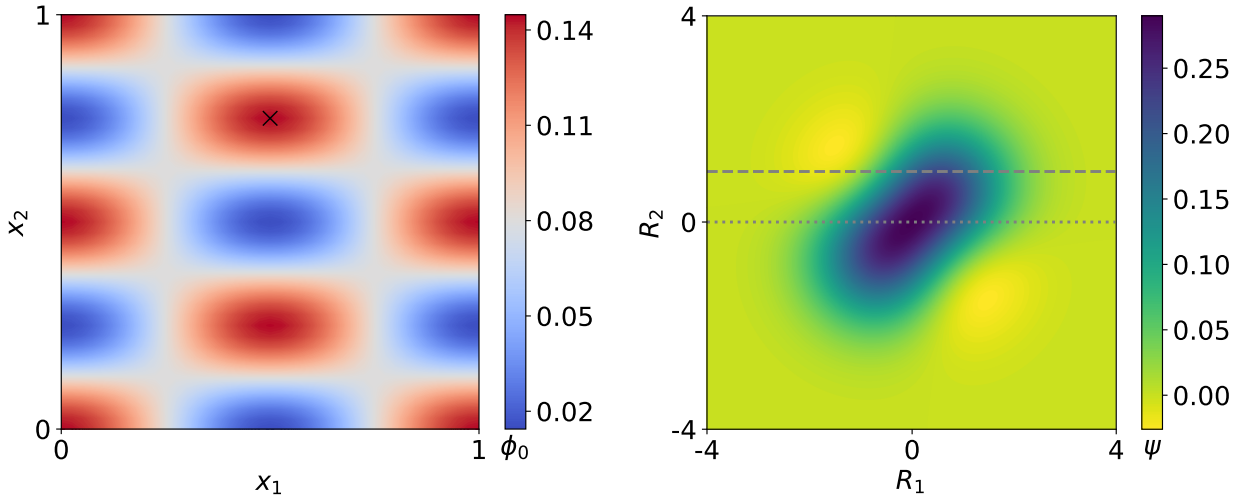

(a) ϕ_0 in the spatial domain Ω

(b) ψ in the configuration space $\mathcal{D}$

Figure 3: The solution ψ and ϕ_0 over the configuration space and the spatial domain at $t = 0.01$, respectively. The black cross in (a) marks the position $(0.5, 0.75)$ in the spatial domain, which is considered for (b) and Figure 4. The dashed and dotted lines in (b) show the positions of the cutouts displayed in the figures 4a and 4b.

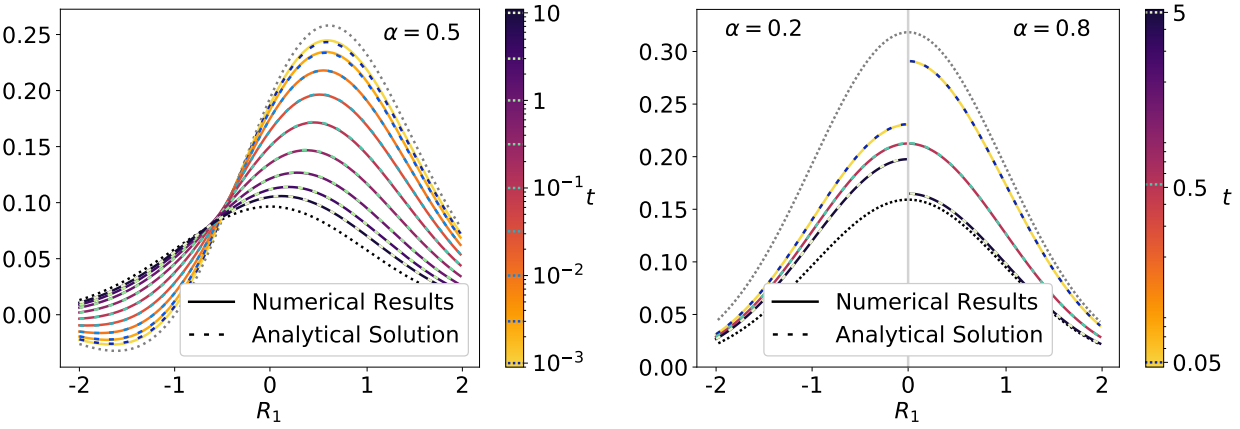

(a) $\alpha = 0.5$

(b) Comparison of $\alpha = 0.2$ and $\alpha = 0.8$

Figure 4: The evolution of the solution ψ is displayed over time for different values of α. We consider the solution at the point $\mathbf{x} = (0.5, 0.75)$ and along the lines visualized in Figure 3b: $R_2 = 1$ (dashed) and $R_2 = 0$ (dotted). Figure (a) displays the evolution over time for $\alpha = 0.5$ along the line $R_2 = 1$ at various time steps. Figure (b) compares the evolution over time for $\alpha = 0.2$ and $\alpha = 0.8$ along the line $R_2 = 0$. The grey dotted line displays the initial condition and the black dotted line the steady state.

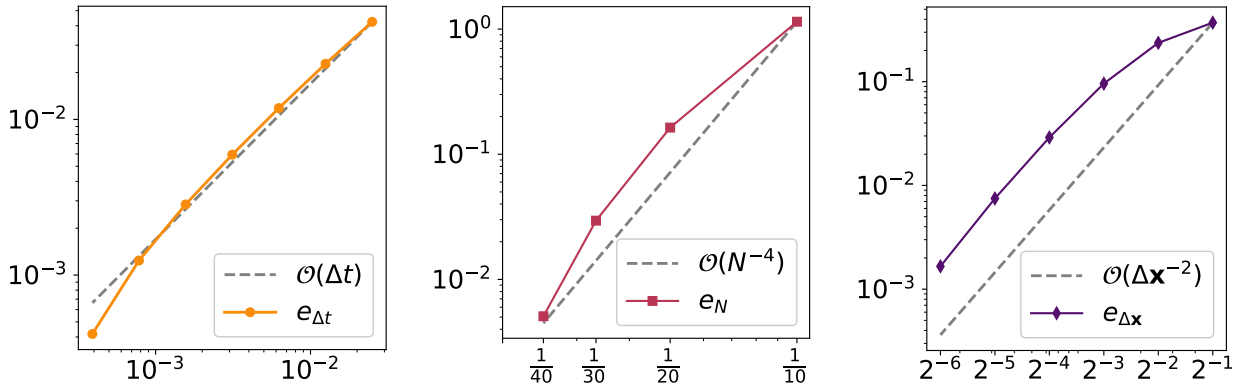

(a) Error decay with respect to Δt (b) Error decay with respect to N (c) Error decay with respect to Δx

Figure 5: Convergence behavior of the numerical method. The solutions for different resolutions are compared with a finer reference solution. While one parameter varies, the other two are fixed to $\Delta t = 0.01$, $N = 10$, and $\Delta \mathbf{x} = 0.125$.

the course of the simulation. This behavior is expected because of the singularity of the integral kernel at $t = 0$ and the fact that the rational approximation is calculated for the interval $[\Delta t, T]$.

We compare the evolution over time of the solutions for $\alpha = 0.2$ and $\alpha = 0.8$ in Figure 4b for $t = 0.05, 0.52, 5$. The displayed solutions are axisymmetric with respect to $R_1 = 0$, and we show the case $\alpha = 0.2$ on the left and $\alpha = 0.8$ on the right. For $\alpha = 0.2$, the solution deviates faster from the initial datum than for $\alpha = 0.8$. At $t = 0.52$, the solutions are nearly identical for the two values of α. For larger t, the solution for $\alpha = 0.8$ approaches the steady state faster and thus overtakes the solution for $\alpha = 0.2$ throughout the simulation. This behavior is typical of the Mittag–Leffler function. The smaller α, the faster the solution deviates from the initial datum and the slower the decay to the steady state.

6.2.2. Convergence behavior of the numerical method

In this section, we investigate the convergence behavior of our numerical method. A detailed comparison with an analytical solution for all three parameters Δt, N, and Δx simultaneously is not feasible because of the high dimensionality of the problem. Therefore, we fix two parameters and compare the solutions for different resolutions for the third parameter. If fixed, we consider $\Delta t = 0.01$, $N = 10$, and $\Delta \mathbf{x} = 0.125$. All simulations are considered on the unit square $\Omega = (0, 1)^2$, $T = 1$, and $m = 20$.

For the time integration, we take the velocity field $\mathbf{u} = (0, 0)$ and the initial datum is chosen to be $\psi_0(\mathbf{x}, \mathbf{R}) = ce^{-\frac{|\mathbf{R}|^2}{2}}(1 + R_1 R_2)$, where again $\mathbf{R} = (R_1, R_2)$ with $R_1, R_2 \in \mathbb{R}$. We consider the time step sizes $\Delta t \in \{0.1 * 2^{-i} \,|\, 0 \leq i \leq 8\}$, while the reference solution $\overline{\psi_{\Delta t}}$ is calculated for $\Delta t = 0.1 * 2^{-9}$, and we define

$$e_{\Delta t} = \int_0^T \left\| \psi_{\Delta t} - \overline{\psi_{\Delta t}} \right\|_{L^2(\mathcal{D})} dt. \tag{63}$$

Note that due to the setting considered, $e_{\Delta t}$ is constant with respect to the spatial variable $\mathbf{x}$. The error decay over the size of the time steps is displayed in Figure 5a. We observe a linear decay, which is expected for the numerical method because we are using the implicit Euler method in conjunction with first-order

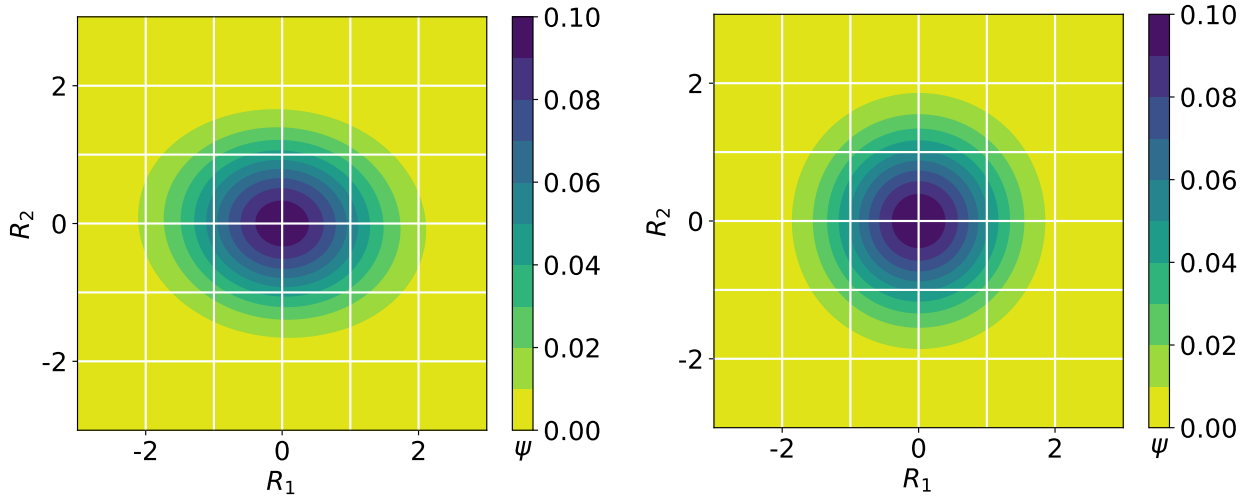

(a) $\tau(\mathbf{u}) = \nabla_{\mathbf{x}}\mathbf{u}$

(b) $\tau(\mathbf{u}) = \frac{1}{2}\left(\nabla_{\mathbf{x}}\mathbf{u} - (\nabla_{\mathbf{x}}\mathbf{u})^{\mathrm{T}}\right)$

Figure 6: Comparison of ψ for the general noncorotational and corotational formulations. The velocity field is set to $\mathbf{u} = \frac{1}{2}(x_1, -x_2)$. The solution ψ is displayed at $t = 0.5$ and $\mathbf{x} = (0.5, 0.5)$.

Strang splitting.

To test the Hermite spectral method, we chose the velocity field $\mathbf{u} = (0, 0)$ and the initial datum is set to $\psi_0(\mathbf{x}, \mathbf{R}) = ce^{-\frac{|\mathbf{R}|^2}{2}}$. We compare the numerical results for $N = 10, 20, 30, 40$ and, for the reference solution $\overline{\psi_N}$, $N = 50$. We consider

$$e_N = \int_0^T \left\|\psi_N - \overline{\psi_N}\right\|_{L_2(\mathcal{D})} dt. \tag{64}$$

The error decay is displayed in Figure 5b. Since the accuracy of the approximation with Hermite polynomials is highly dependent on the shape of the approximated function and the choice of the parameter a, this convergence behavior cannot be assumed for arbitrary initial data and velocity fields [51].

For the discretization of the spatial domain, the velocity field $\mathbf{u} = \frac{1}{2}(x_1, -x_2)$ and the initial datum is set to $\psi_0(\mathbf{x}, \mathbf{R}) = ce^{-\frac{|\mathbf{R}|^2}{2}}$. For the reference solution $\overline{\psi_{\Delta\mathbf{x}}}$, we set $\Delta\mathbf{x} = 2^{-8}$ and compare the solutions for $\Delta\mathbf{x} \in \{2^{-1}, \ldots, 2^{-7}\}$. We consider

$$e_{\Delta\mathbf{x}} = \int_0^T \left\|\phi_{0,\Delta\mathbf{x}} - \overline{\phi_{0,\Delta\mathbf{x}}}\right\|_{L_2(\Omega)} dt. \tag{65}$$

The error decay in Figure 5c shows the expected quadratic behavior.

6.2.3. Influence of the velocity field

In the following, we investigate the influence of the drag term $\tau(\mathbf{u})$ for the velocity field $\mathbf{u} = \frac{1}{2}(x_1 + x_2, -x_1 - x_2)$. We consider $\alpha = 0.5$, $m = 20$, $\Delta t = 0.001$, $N = 10$, $\Delta\mathbf{x} = 0.0625$, and consider the initial datum $\psi_0(\mathbf{x}, \mathbf{R}) = ce^{-\frac{|\mathbf{R}|^2}{2}}$, where again c is a normalizing factor. Thus, the initial datum is rotationally symmetric with respect to $\mathbf{R}$. The full gradient and its skew-symmetric part appearing in the general

noncorotational and corotational drag term, respectively, are given by

$$\nabla_{\mathbf{x}}\mathbf{u} = \frac{1}{2}\begin{pmatrix} 1 & 1 \\ -1 & -1 \end{pmatrix}, \quad \frac{1}{2}\left(\nabla_{\mathbf{x}}\mathbf{u} - (\nabla_{\mathbf{x}}\mathbf{u})^{\mathrm{T}}\right) = \frac{1}{2}\begin{pmatrix} 0 & 1 \\ -1 & 0 \end{pmatrix}. \tag{66}$$

Figure 6a shows ψ over the configuration space for the general noncortational model. We observe stretching of ψ along the main axes and a rotation. A positive value on the diagonal of $\tau(\mathbf{u})$ corresponds to extension along the respective axis, while a negative value corresponds to compression. The off-diagonal entries of $\tau(\mathbf{u})$ determine the extent of rotation. For the corotational case, the diagonal entries of $\tau(\mathbf{u})$ vanish, and thus, the rotational symmetry of the initial condition is preserved, see Figure 6b.

6.3. Simulation of the time-fractional Navier-Stokes-Fokker-Planck equation

For the TFNSFP system we consider as our test problem flow through a channel with a half-disc cut out from its lower half. Based on this scenario, we study the influence of α on the velocity profile, the convergence behavior of our method, the influence of the polynomial degree N in the Hermite spectral method, and the difference between the general noncorotational case and the corotational formulation.

The rectangular spatial domain with a circular cut-out with center $(1.5, 0)$ and radius 0.5 measures 3 by 1. It is displayed in Figure 9. Along the left vertical edge of the domain, we consider a time-dependent, quadratic inflow profile $\mathbf{u} = ((1 - x_2)x_2(1 - \cos(2\pi t)), 0)$. Over the first half of the simulation, the velocity profile increases to double its initial value and decreases again to zero over the second half. For the top and the bottom, including the circular arc, we set $\mathbf{u} = (0, 0)$ and consider a zero-stress boundary condition along the right vertical edge of the domain. Note that in this scenario, the polymer number density is not constant in space. Thus, from a physical point of view, γ in the definition of $\mathbf{T}$ should be dependent on the spatial variable. The domain is discretized into 5951 triangles. Unless stated otherwise, the parameters in the simulation are set to $\xi = \chi = \epsilon = 1$, $\nu = 0.59$, $T = 1$, $N = 2$, $m = 20$, and $\Delta t = 0.00015625$. To visualize the influence of the coupling tensor, it is scaled by a factor of 5. We choose the initial velocity $\mathbf{u}_0 = \mathbf{0}$ and set $\psi_0 = ce^{-\frac{|\mathbf{R}|^2}{2}}$. Thus, ψ_0 is the steady state solution of the TFFPE for the initial velocity field $\mathbf{u}_0$. Since ψ_0 is rotationally symmetric and independent of the spatial variable $\mathbf{x}$, the $\mathbf{x}$-divergence of the coupling Kramers tensor appearing on the right-hand side of the NSE vanishes at $t = 0$.

6.3.1. Influence of α

We compare the velocity field for different values of α in Figure 9. The image shows $\|\mathbf{u}\|_2$ at the times $t = 0.01, 0.95$, and 0.98. The numerical results indicate that the $\alpha = 0.3$ case adapts the fastest to the change in the inflow profile, while the other two cases are similar at $t = 0.01$. During the simulation, the inflow increases and the differences between the velocities are negligible. At the end of the simulation, the velocity fields are larger for smaller values of α, indicating more significant memory effects.

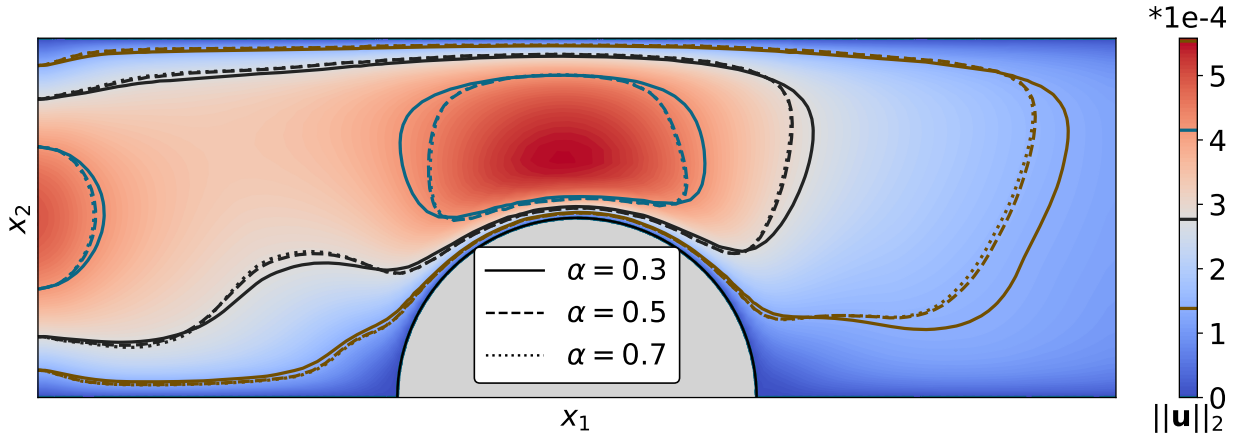

(a) $t = 0.01$

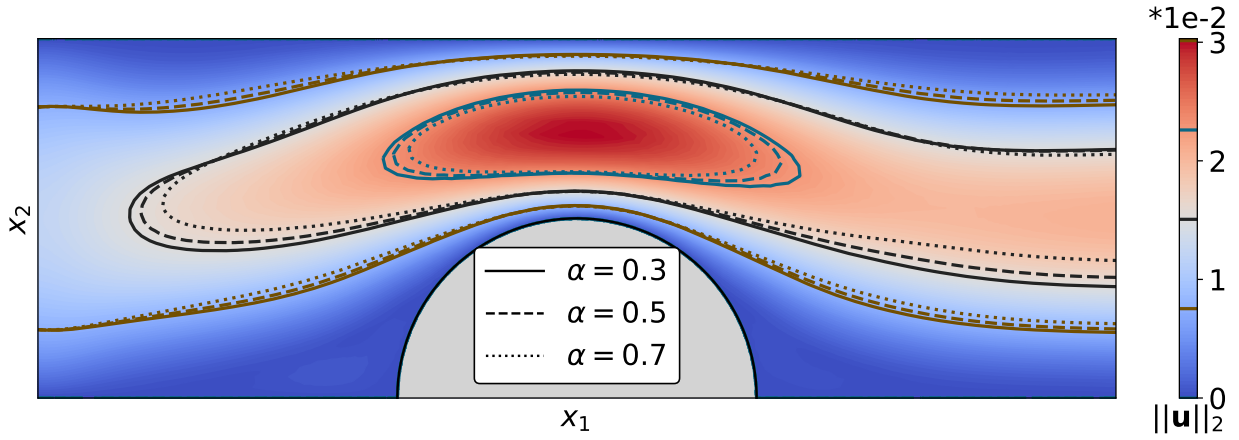

(b) $t = 0.95$

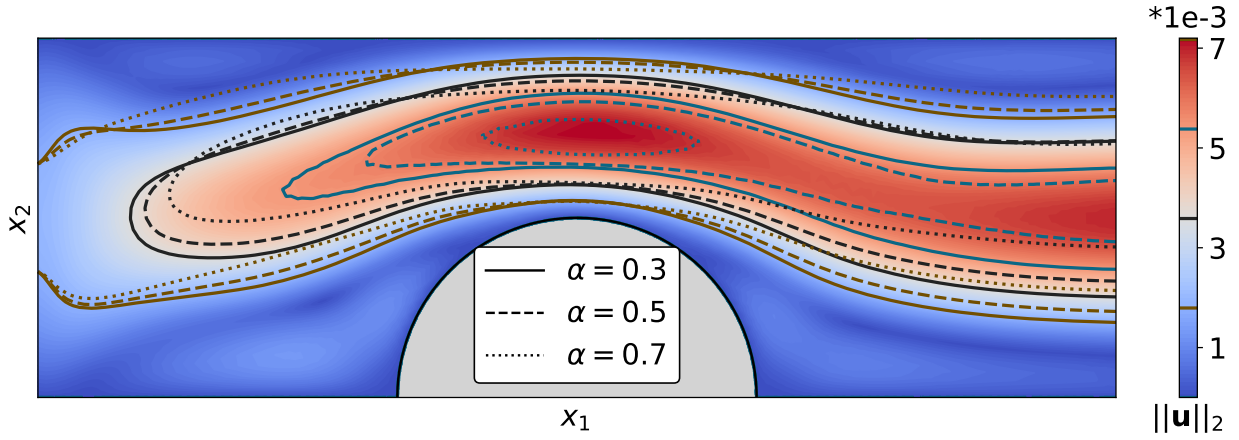

(c) $t = 0.98$

Figure 7: The velocity field is shown for $\alpha \in \{0.3, 0.5, 0.7\}$ at the times $t \in \{0.01, 0.95, 0.98\}$. The background displays the velocity field for $\alpha = 0.3$, and the contour lines visualize the difference between the velocity field for the three different alpha values. In each subfigure, the contour lines represent the same values independent of the value of α.

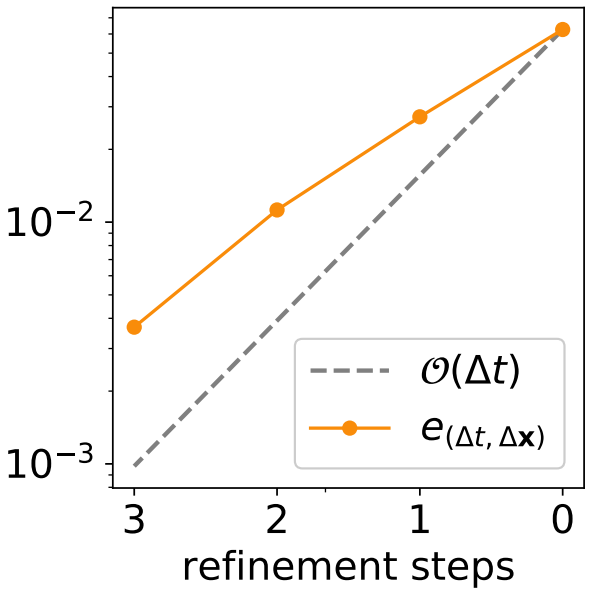

Figure 8: Error decay with respect to simultaneously refinement of Δt and $\Delta \mathbf{x}$

6.3.2. Convergence behavior

The error decay for simultaneous refinement of the discretization in space and time is visualized in Figure 8. As discussed in Section 5, the polynomial degree in the Hermite spectral method does not influence the accuracy of $\mathbf{u}$ and p. The time step size of the ith refinement step is given by $\Delta t = 0.01 * 4^{-i}$. For the spatial discretization, we consider $\Delta \mathbf{x} = \Delta \mathbf{x}_0 * 2^{-i}$. The error is defined as

$$e_{(\Delta t, \Delta \mathbf{x})} = \int_0^T \|\mathbf{u} - \overline{\mathbf{u}}\|_{L_2(\Omega)} \, dt, \tag{67}$$

where $\overline{\mathbf{u}}$ is the reference solution calculated using 4 refinement steps.

6.3.3. Influence of N

As discussed in Section 5, the degree of the Hermite spectral method only influences the accuracy of ψ, and $N = 2$ is sufficient to determine the velocity field and the pressure. In Figure 9a, we compare the coupling tensor for $N = 2$ and $N = 9$ in the form of $\mathbf{G} := \| \int_{\mathcal{D}} (\psi_2 - \psi_9) \mathbf{R}\mathbf{R}^{\mathrm{T}} d\mathbf{R} \|_{L^2(\Omega)}$; here, for the sake of avoiding notational confusion, we note that the norm $\|\cdot\|_{L^2(\Omega)}$ has been applied componentwise to the tensor appearing under the norm sign, which is why $\mathbf{G}$, thus defined, is a tensor (with nonnegative components). The tensor $\mathbf{G}$ is obtained by numerically integrating over the configuration space $\mathcal{D}$ without exploiting the structure described in equation (60). The numerical results show that the components of $\mathbf{G}$ vanish, thus validating the theoretical result that $N = 2$ is sufficient to determine the velocity and pressure.

6.3.4. Influence of the drag term $\tau(\mathbf{u})$

In the setting of Lemma 2, i.e., by considering a homogeneous natural (Neumann) boundary condition on $\partial\Omega$, the datum taken to be rotationally symmetric with respect to $\mathbf{R}$ and independent of the spatial variable

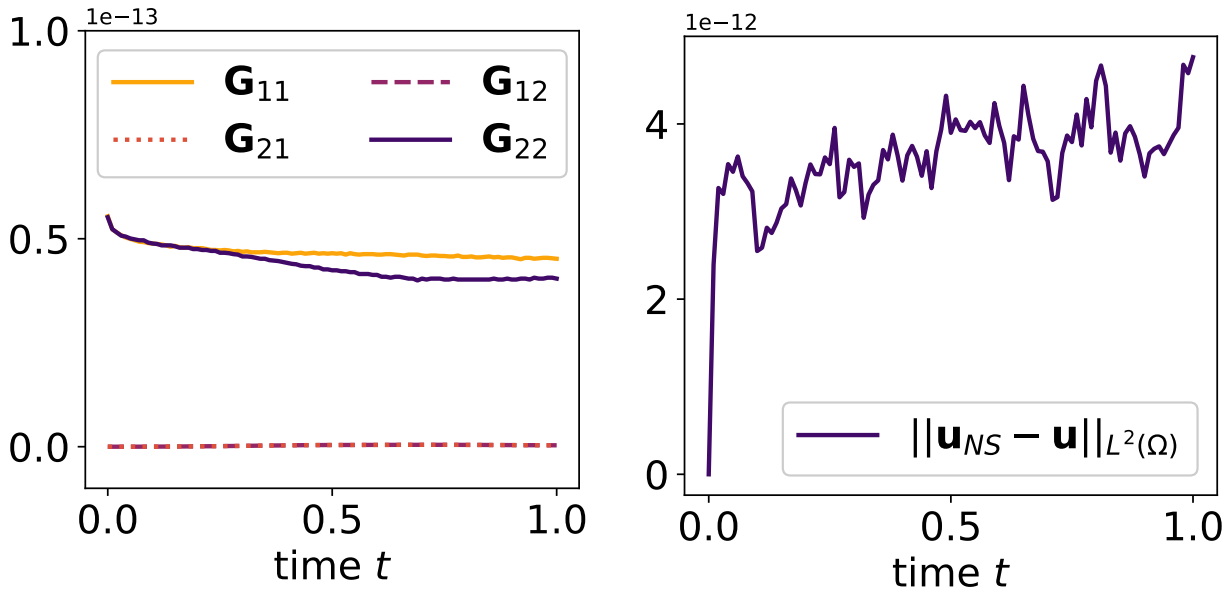

(a) Components of $\mathbf{G} \coloneqq \left\| \int_{\mathcal{D}} (\psi_2 - \psi_9) \mathbf{R}\mathbf{R}^{\mathrm{T}} d\mathbf{R} \right\|_{L^2(\Omega)}$.

(b) Comparison of the velocity fields $\mathbf{u}_{NS}$ and $\mathbf{u}$.

Figure 9: (a) Comparison of the coupling tensors for $N = 2$ and $N = 9$. (b) Comparison of the velocity fields of the NSE and the TFNSFP system in the setting of Lemma 2.

$\mathbf{x}$, and consider the corotational formulation $\tau(\mathbf{u}) = \frac{1}{2}\left(\nabla_{\mathbf{x}}\mathbf{u} - (\nabla_{\mathbf{x}}\mathbf{u})^{\mathrm{T}}\right)$. The TFNSFP system decouples. Thus, the velocity field and the pressure can be calculated independently of ψ. In Figure 9b, we compare the velocity field $\mathbf{u}$ of the TFNSFP system in the setting of Lemma 2 to the velocity field of the NSE $\mathbf{u}_{NS}$ without coupling. The differences between the results for the pure NSE and the TFNSFP system are in the range of 10^{-12}, validating our theoretical finding that the Navier–Stokes system is completely decoupled from the corotational Fokker–Planck equation when the initial datum for the latter is rotationally symmetric with respect to $\mathbf{R}$ and independent of $\mathbf{x}$, so the velocity and the pressure are not influenced by ψ.

7. Conclusion

In this work, we presented a numerical scheme for the time-fractional Fokker–Planck equation coupled to the incompressible Navier–Stokes equations. The system of partial differential equations under consideration arises in models of dilute polymeric fluids. The time-fractional derivative appearing in the Fokker–Planck equation was discretized using a rational approximation, which decomposes the time-fractional differential equation into a fixed number, m, of integer-order differential equations. While for the sake of simplicity we took m to have a fixed value in this work, the accuracy of the approximation of the integral kernel depends on m, α, and the length of the time interval under consideration.

We transformed the $2d$-dimensional Fokker–Planck equation, with $d \in \{2, 3\}$, into its configuration space part posed on $\mathcal{D} = \mathbb{R}^d$ and its physical domain part posed on the flow domain $\Omega \subset \mathbb{R}^d$, and discretized the problems with a Hermite spectral method and an $H^1(\Omega)$-conforming finite element method, respectively. For

the problem posed on the configuration space domain $\mathcal{D}$, at each vertex of the triangulated spatial domain, Ω, we solved a system of $(N+1)^d$ ordinary differential equations, where N denotes the (highest) polynomial degree in the Hermite spectral basis used. For the problem posed on the physical/spatial domain, Ω, we solved a d-dimensional advection-diffusion equation for each spectral mode of the Hermite spectral method. The solutions of the subproblems can be calculated separately and in parallel.

We showed that the algebraic structure of the discretized configuration space part problem of the Fokker–Planck equation decouples into block lower tridiagonal matrices, and therefore the resulting system of algebraic equations can be solved using a forward substitution on the block matrices. Further, we presented a new numerical approach to compute the velocity field and the pressure from the time-fractional Navier–Stokes–Fokker–Planck system without fully resolving the Fokker–Planck equation. For $d = 2$ ($d = 3$), we only have to solve a coupled two-dimensional (three-dimensional) system of 4 (7) time-fractional partial differential equations instead of the inherently four-dimensional (six-dimensional) time-fractional Fokker–Planck equation. In the setting of a constant polymer number density the system size is even further reduced to 3 (6). Our approach significantly reduces the computational cost and is also an attractive candidate for future three-dimensional simulations.

The corotational version of the Fokker–Planck equation has been widely studied in the literature. We have shown that the corotational time-fractional Fokker–Planck equation preserves rotational symmetry if the initial datum is rotationally symmetric. Additionally, we showed that, if the initial datum is identically constant as a function of $\mathbf{x} \in \Omega$, then the time-fractional Navier–Stokes–Fokker–Planck system decouples. For the sake of simplicity our proofs were presented in the case of two space dimensions, but these results can be generalized to three space dimensions and were confirmed by means of numerical simulations.

We performed numerical experiments for the time-fractional Fokker–Planck equation that show differing evolution over time for different values of α. The smaller the value of α, the faster the solution deviates from the initial datum, but the slower it finally progresses towards steady state. This corresponds to the time-decay of the Mittag–Leffler function. Further simulations for the time-fractional Navier–Stokes–Fokker–Planck system demonstrate the influence of the coupling. The order of the time-fractional derivative does not only influence the solution of the Fokker–Planck equation, but also the velocity field and the pressure. This illustrates the presence of memory effects induced by the time-fractional derivative appearing in the Fokker–Planck equation in this class of models of dilute polymeric fluids.

To the best of our knowledge the existence and uniqueness of a solution to the time-fractional Navier–Stokes–Fokker–Planck system for $\alpha \in (0, 1)$ in the general noncorotational case, and for $\alpha \in (0, \frac{1}{2})$ for the corotational formulation, are open theoretical questions. Besides the analysis and numerical analysis of the system, other logical future steps include the transition from the Hookean spring model considered here to the FENE model, the inclusion of more general coupling terms, the development of structure-preserving numerical methods, as well as three-dimensional simulations.

8. Acknowledgement

The authors would like to thank anonymous reviewers for their helpful suggestions, which led to the improvement of this article. BW and JB gratefully acknowledges the support of the German Science Foundation (DFG) for funding part of this work through grant WO 671/11-1.

References

[1] A. Groisman, V. Steinberg, Elastic turbulence in a polymer solution flow, Nature 405 (6782) (2000) 53–55.

[2] D. D. Joseph, Fluid dynamics of viscoelastic liquids, Vol. 84, Springer Science & Business Media, 2013.

[3] A. D. Fokker, Die mittlere Energie rotierender elektrischer Dipole im Strahlungsfeld, Annalen der Physik 348 (5) (1914) 810–820.

[4] M. Planck, Sitzungsber, Preuss. Akad. Wiss. Phys. Math. Kl 325 (3).

[5] L.-D. Chang, D. Waxman, Quantum Fokker–Planck equation, Journal of Physics C: Solid State Physics 18 (31) (1985) 5873.

[6] H. Carmichael, Statistical methods in quantum optics 1: master equations and Fokker-Planck equations, Vol. 1, Springer Science & Business Media, 1999.

[7] N. G. Van Kampen, Stochastic processes in physics and chemistry, Vol. 1, Elsevier, 1992.

[8] J. La, On Diffusive 2D Fokker–Planck–Navier–Stokes Systems, Archive for Rational Mechanics and Analysis 235 (3) (2020) 1531–1588.

[9] M. Renardy, B. Thomases, A mathematician's perspective on the Oldroyd B model: Progress and future challenges, Journal of Non-Newtonian Fluid Mechanics 293 (2021) 104573.

[10] J. W. Barrett, E. Süli, Existence of global weak solutions to finitely extensible nonlinear bead–spring chain models for dilute polymers with variable density and viscosity, Journal of Differential Equations 253 (12) (2012) 3610–3677.

[11] E. Feireisl, Y. Lu, E. Süli, Dissipative weak solutions to compressible Navier–Stokes–Fokker–Planck systems with variable viscosity coefficients, Journal of Mathematical Analysis and Applications 443 (1) (2016) 322–351.

[12] H. Mizerová, B. She, A conservative scheme for the Fokker–Planck equation with applications to viscoelastic polymeric fluids, Journal of Computational Physics 374 (2018) 941–953.

[13] J. W. Barrett, E. Süli, Existence of global weak solutions to the kinetic Hookean dumbbell model for incompressible dilute polymeric fluids, Nonlinear Analysis: Real World Applications 39 (2018) 362–395.

[14] P. Gwiazda, M. Lukáčová-Medvidová, H. Mizerová, A. Świerczewska Gwiazda, Existence of global weak solutions to the kinetic Peterlin model, Nonlinear Analysis: Real World Applications 44 (2018) 465–478.

[15] J. Barrett, E. Süli, Existence of global weak solutions to Fokker-Planck and Navier-Stokes-Fokker-Planck equations in kinetic models of dilute polymers, Discrete & Continuous Dynamical Systems - S 3 (3) (2010) 371–408.

[16] J. W. Barrett, E. Süli, Existence of global weak solutions to compressible isentropic finitely extensible nonlinear bead–spring chain models for dilute polymers: The two-dimensional case, Journal of Differential Equations 261 (1) (2016) 592–626.

[17] T. Dębiec, E. Süli, On a class of generalised solutions to the kinetic hookean dumbbell model for incompressible dilute polymeric fluids: existence and macroscopic closure, arXiv preprint arXiv:2306.16901.

[18] P.-L. Lions, N. Masmoudi, Global existence of weak solutions to some micro-macro models, Comptes Rendus Mathematique 345 (1) (2007) 15–20.

[19] N. Masmoudi, P. Zhang, Z. Zhang, Global well-posedness for 2D polymeric fluid models and growth estimate, Physica D: Nonlinear Phenomena 237 (10-12) (2008) 1663–1675.

[20] N. Masmoudi, Well-posedness for the FENE dumbbell model of polymeric flows, Communications on Pure and Applied Mathematics: A Journal Issued by the Courant Institute of Mathematical Sciences 61 (12) (2008) 1685–1714.

[21] M. E. Schonbek, Existence and decay of polymeric flows, SIAM Journal on Mathematical Analysis 41 (2) (2009) 564–587.

[22] J. W. Barrett, E. Süli, Numerical approximation of corotational dumbbell models for dilute polymers, IMA Journal of Numerical Analysis 29 (4) (2009) 937–959.

[23] T. Dębiec, E. Süli, Corotational Hookean models of dilute polymeric fluids: Existence of global weak solutions, weak-strong uniqueness, equilibration, and macroscopic closure, SIAM Journal on Mathematical Analysis 55 (1) (2023) 310–346.

[24] A. Lozinski, C. Chauvière, A fast solver for Fokker–Planck equation applied to viscoelastic flows calculations: 2D FENE model, Journal of Computational Physics 189 (2) (2003) 607–625.

[25] D. J. Knezevic, E. Süli, A heterogeneous alternating-direction method for a micro-macro dilute polymeric fluid model, ESAIM: Mathematical Modelling and Numerical Analysis 43 (6) (2009) 1117–1156.

[26] D. J. Knezevic, E. Süli, Spectral Galerkin approximation of Fokker-Planck equations with unbounded drift, ESAIM: Mathematical Modelling and Numerical Analysis 43 (3) (2009) 445–485.

[27] J. Fok, B. Guo, T. Tang, Combined Hermite spectral-finite difference method for the Fokker–Planck equation, Mathematics of Computation 71 (240) (2002) 1497–1528.

[28] C. Duan, W. Chen, C. Liu, X. Yue, S. Zhou, Structure-Preserving Numerical Methods for Nonlinear Fokker–Planck Equations with Nonlocal Interactions by an Energetic Variational Approach, SIAM Journal on Scientific Computing 43 (1) (2021) B82–B107.

[29] L. Pareschi, M. Zanella, Structure Preserving Schemes for Nonlinear Fokker–Planck Equations and Applications, Journal of Scientific Computing 74 (3) (2018) 1575–1600.

[30] M. Fritz, E. Süli, B. Wohlmuth, Analysis of a dilute polymer model with a time-fractional derivative (2023). arXiv:2307.16606.

[31] E. Heinsalu, M. Patriarca, I. Goychuk, P. Hänggi, Use and abuse of a fractional Fokker–Planck dynamics for time-dependent driving, Physical Review Letters 99 (12) (2007) 120602.

[32] K. Diethelm, The Analysis of Fractional Differential Equations: An Application-Oriented Exposition Using Differential Operators of Caputo Type, Springer Berlin Heidelberg, Berlin, Heidelberg, 2010.

[33] K. Oldham, J. Spanier, The fractional calculus theory and applications of differentiation and integration to arbitrary order, Elsevier, 1974.

[34] B. Jin, R. Lazarov, Z. Zhou, An analysis of the L1 scheme for the subdiffusion equation with nonsmooth data, IMA Journal of Numerical Analysis 36 (1) (2016) 197–221.

[35] C. Lubich, On the stability of linear multistep methods for Volterra convolution equations, IMA Journal of Numerical Analysis 3 (4) (1983) 439–465.

[36] K. Diethelm, N. J. Ford, A. D. Freed, A Predictor-Corrector Approach for the Numerical Solution of Fractional Differential Equations, Nonlinear Dynamics 29 (1) (2002) 3–22.

[37] G. Beylkin, L. Monzón, On approximation of functions by exponential sums, Applied and Computational Harmonic Analysis 19 (1) (2005) 17–48.

[38] W. McLean, Exponential sum approximations for $t^{-\beta}$, in: Contemporary Computational Mathematics-A Celebration of the 80th Birthday of Ian Sloan, Springer, 2018, pp. 911–930.

[39] D. Baffet, J. S. Hesthaven, A Kernel Compression Scheme for Fractional Differential Equations, SIAM Journal on Numerical Analysis 55 (2) (2017) 496–520.

[40] K. Diethelm, R. Garrappa, M. Stynes, Good (and not so good) practices in computational methods for fractional calculus, Mathematics 8 (3) (2020) 324.

[41] W. R. Schneider, W. Wyss, Fractional diffusion and wave equations, Journal of Mathematical Physics 30 (1) (1989) 134–144.

[42] W. Deng, Numerical algorithm for the time fractional Fokker–Planck equation, Journal of Computational Physics 227 (2) (2007) 1510–1522.

[43] Z. Odibat, S. Momani, Numerical solution of Fokker–Planck equation with space- and time-fractional derivatives, Physics Letters A 369 (5) (2007) 349–358.

[44] W. Deng, Finite element method for the space and time fractional Fokker—Planck equation, SIAM Journal on Numerical Analysis 47 (1) (2009) 204–226.

[45] S. Vong, Z. Wang, A high order compact finite difference scheme for time fractional Fokker–Planck equations, Applied Mathematics Letters 43 (2015) 38–43.

[46] Y. Jiang, X. Xu, A monotone finite volume method for time fractional Fokker–Planck equations, Science China Mathematics 62 (4) (2019) 783–794.

[47] S. Momani, O. A. Arqub, A. Freihat, M. Al-Smadi, Analytical approximations for Fokker–Planck equations of fractional order in multistep schemes, Applied and Computational Mathematics 15 (3) (2016) 319–330.

[48] A. M. S. Mahdy, Numerical solutions for solving model time-fractional Fokker–Planck equation, Numerical Methods for Partial Differential Equations 37 (2) (2021) 1120–1135.

[49] F. Mainardi, Fractional calculus and waves in linear viscoelasticity: an introduction to mathematical models, World Scientific, 2022.

[50] J. Shen, T. Tang, L.-L. Wang, Spectral methods: algorithms, analysis and applications, Vol. 41, Springer Science & Business Media, 2011.

[51] D. Gottlieb, S. A. Orszag, 3. Survey of Approximation Theory, in: Numerical Analysis of Spectral Methods, CBMS-NSF Regional Conference Series in Applied Mathematics, Society for Industrial and Applied Mathematics, 1977, pp. 21–45.

[52] M. Mohammadi, A. Borzi, A Hermite spectral method for a Fokker–Planck optimal control problem in an unbounded domain, International Journal for Uncertainty Quantification 5 (3).

[53] U. Khristenko, B. Wohlmuth, Solving time-fractional differential equations via rational approximation, IMA Journal of Numerical Analysis (2022) 1263–1290.

[54] S. Bernstein, Sur les fonctions absolument monotones, Acta Mathematica 52 (1) (1929) 1–66.

[55] Y. Nakatsukasa, O. Sète, L. N. Trefethen, The AAA algorithm for rational approximation, SIAM Journal on Scientific Computing 40 (3) (2018) A1494–A1522.

[56] G. Strang, On the construction and comparison of difference schemes, SIAM Journal on Numerical Analysis 5 (3) (1968) 506–517.

[57] R. I. McLachlan, G. R. W. Quispel, Splitting methods, Acta Numerica 11 (2002) 341–434.

[58] C. Chauvière, A. Lozinski, Simulation of dilute polymer solutions using a Fokker–Planck equation, Computers & fluids 33 (5-6) (2004) 687–696.

[59] J. Shen, L.-L. Wang, Some recent advances on spectral methods for unbounded domains, Communications in Computational Physics 5 (2-4) (2009) 195–241.

[60] A. J. Chorin, A numerical method for solving incompressible viscous flow problems, Journal of Computational Physics 2 (1) (1967) 12–26.

[61] A. J. Chorin, Numerical solution of the navier-stokes equations, Mathematics of Computation 22 (104) (1968) 745–762.

[62] J.-L. Guermond, P. Minev, J. Shen, An overview of projection methods for incompressible flows, Computer Methods in Applied Mechanics and Engineering 195 (44-47) (2006) 6011–6045.

[63] M. Franco, J.-S. Camier, J. Andrej, W. Pazner, High-order matrix-free incompressible flow solvers with GPU acceleration and low-order refined preconditioners, Computers & Fluids 203 (2020) 104541.

[64] A. G. Tomboulides, J. C. Y. Lee, S. A. Orszag, Numerical Simulation of Low Mach Number Reactive Flows, Journal of Scientific Computing 12 (2) (1997) 139–167.

[65] R. Anderson, J. Andrej, A. Barker, J. Bramwell, J.-S. Camier, J. C. V. Dobrev, Y. Dudouit, A. Fisher, T. Kolev, W. Pazner, M. Stowell, V. Tomov, I. Akkerman, J. Dahm, D. Medina, S. Zampini, MFEM: A modular finite element methods library, Computers & Mathematics with Applications 81 (2021) 42–74.